Proximity Sensors

Using Time-of-Flight and Single-Photon Avalanche Diodes

Gregory Kevin Hill

Measuring travel time of infrared photons in well-lit environments

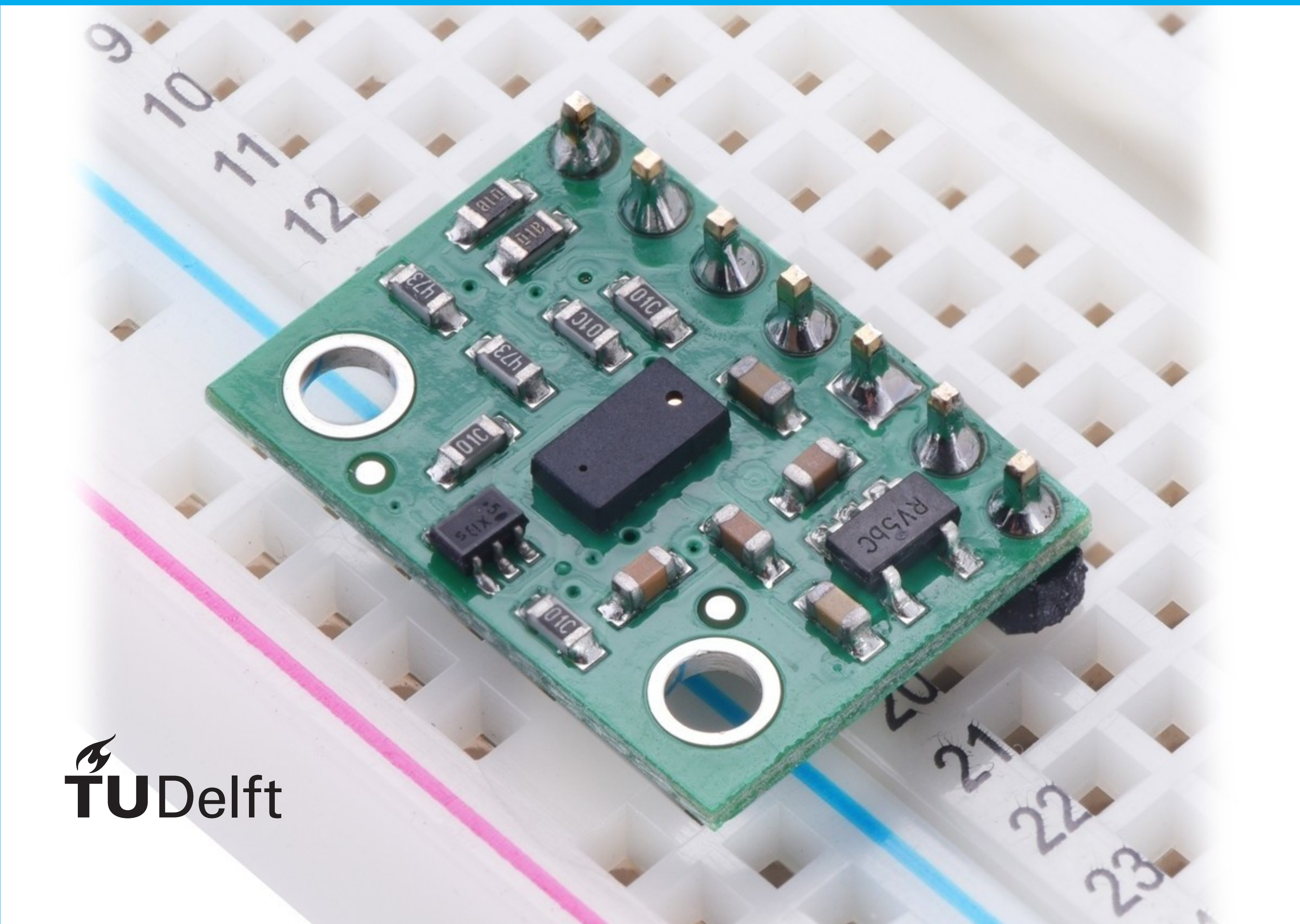

TU Delft

Proximity Sensors

Using Time-of-Flight and Single-Photon Avalanche Diodes

by

Gregory Kevin Hill

to obtain the degree of Master of Science
at the Delft University of Technology,
to be defended publicly on December 10 at 13:30 PM.

Student number:	4287592	
Project duration:	February 11, 2019 – December 10, 2019	
Thesis committee:	Dr. S. Cotofana,	TU Delft, supervisor
	Ir. C. van den Bos,	SystematIC, supervisor
	Dr. F. Sebastiano,	TU Delft
	Dr. S. Wong,	TU Delft

This thesis is confidential and cannot be made public until December 10, 2022.

TU Delft

Abstract

Most current proximity sensing methods fail the stringent requirements of modern smartphones. A position sensing device (PSD) requires a laser placed some distance away from the sensor, intensity-based solutions are sensitive to changes in reflectivity, and ultrasound-based sensors cannot measure small distances because of resonance.

With modern transistors getting smaller and smaller, single-photon detectors have become feasible. Using a single-photon detector called a SPAD and a laser, the travel time of light can be measured. This technique, called time-of-flight, existed for several decades where radar and ultrasound are concerned but only recently includes single-photon detectors.

Several products exist that use single-photon time of flight to measure proximity. However, they are limited in terms of maximum distance, resolution and ambient light tolerance. The question arises what the best possible performance of such a system is. For radar and ultrasound, this has been calculated long ago already, but for time of flight, no such analysis exists. This analysis is the main contribution of this thesis. A formula is calculated that takes all parameters of the system into account and produces an expected standard error. This formula is verified using a simulator. The effect of an increasing opening angle of laser and SPAD is analyzed, as well as different waveforms of the laser, using multiple SPADs in smart ways, and increasing the time of a single measurement. It is shown that when less than a thousand SPADs are used, no smart way of combining hits on different SPADs exists. The waveform emitted by a laser is typically a mix of a sine, a square wave and some effects resembling RC-behavior. The nearer to a square wave this is, the smaller the resulting standard error is.

The most power-hungry aspect of such a proximity sensing solution is often the time discretization device. To obtain a high resolution in the order of millimeters, the time resolution should be in the order of picoseconds. Such an extremely high resolution, below the switching time of a single transistor, can typically only be obtained by trading trade area, power and read-out time for resolution. This thesis analyzes a solution using a low-resolution time-to-digital converter (TDC) and multiple sub-intervals for a shorter time to increase resolution.

Preface

This thesis has been quite a journey. In the past 10 months I've had a couple of good firsts. The first time I actually did 2-3 months of reading in a field of research before doing anything. The first time living a 40-hour week. The first time doing this amount of research. The first time building a proper project in Rust. The first time living with roommates. The first time writing such a large report. It taught me a lot, most importantly that nobody can do this alone. Along the way, a great many friends helped me in various ways, from uncertainties of the future, thesis-stress, disagreements about how often it's normal to have friends over for dinner (Hint: not every day of the week for 5 consecutive weeks), and a lot more.

I want to thank everybody who proofread my thesis, all the people I had over for dinner during these months for cheering me up when I needed it, and everybody from DSZ WAVE, the swimming association, for being an amazingly fun community. Specifically:

Nils, thanks for the many many songs we shared, ranging from "pokkeherrie" to "takkeherrie", keeping each other awake throughout the day, and for checking up on me so often.

Dr. Cotofana, you always had time when I needed it, even though you have an awfully full schedule, you always had time to talk about my problems.

Rens, thanks for being the best and most supportive friend I could ever wish for. Thanks for prying a half-finished thesis from my hands and proofreading it so often, and for your huge amount of high-quality feedback. And thank you for always being there.

Chris, I could not wish for a better supervisor. At every step of the way, whenever I did not see any trees through the forest, you were there to guide me, listen to my ramblings, tell me to back up, sit down, write it out and then come back and explain it properly. And thanks for taking the pressure off with a lot of jokes.

Regarding the thesis, if you have questions, send me an email at `me at kevinhill dot nl`.

"Met twee maten meten is gezelliger dan alleen"
– Anonymous

Gregory Kevin Hill
Delft, December 2019

Contents

List of Figures

List of Tables

Nomenclature

χ_{R}	Reflectivity of target material, see equation (3.2)
λ	Wavelength of photons, see equation (3.3)
τ_{tdc}	Resolution of the time-to-digital converter, see equation (3.22)
θ	Opening angle of laser and SPAD, see equation (3.1)
A_{SPAD}	Light-sensitive area of the SPAD, see equation (3.2)
B	Amount of bins in histogram, see equation (3.22)
c	Speed of light through vacuum, see equation (3.3)
d	Distance between SPAD and wall/target, see equation (3.2)
E_{photon}	Energy of a photon, see equation (3.3)
h	Planck constant, see equation (3.3)
I_{a}	Intensity of ambient light, see equation (3.27)
N_{SPAD}	Number of SPADs in use, see equation (3.27)
P_{pd}	Photon detection probability, see equation (3.4)
P_{r}	Optical power arriving at SPAD, see equation (3.2)
P_{t}	Optical power transmitted by laser, see equation (3.2)
Q_{x}	The amount of photons in a bin due to phenomenon x with arrival rate R_x, see equation (3.23)
R_{laser}	The detectable photon arrival rate at a SPAD due to the laser power source, see equation (3.1)
R_{noise}	The detectable photon arrival rate at a SPAD due to ambient photons, see equation (3.1)
R_{total}	The total detectable photon arrival rate at a SPAD, see equation (3.1)
T_L	Oscillation frequency of the laser, see equation (3.22)

Acronyms

ADC Analog to digital converter.
ASIC Application-specific integrated circuit.

CMOS Complementary metal-oxide semiconductor.
CPU Central processing unit.

DCR Dark count rate.
DNL Differential nonlinearity.
dToF Direct time of flight.

FMA Fused multiply-add.
FPGA Field programmable gate array.

GPGPU General-purpose computing on graphics processing units.
GPU Graphics processing unit.

IC Integrated circuit.
INL Integral nonlinearity.
iToF Indirect time of flight.

LED Light emitting diode.
LSB Least significant bit.

PSD Position sensing device.

radar Radio detection and ranging.

SAR Successive approximation register.
SMARTS Simple Model of Atmospheric Radiative Transfer of Sunshine [1].
SNR Signal to noise ratio.
SPAD Single-photon avalanche diode.

TDC Time-to-digital converter.
ToF Time of flight.

VCSEL Vertical-cavity surface-emitting laser [2].

1 Introduction

Modern smartphones contain many sensors performing a wide range of activities, such as:

- Dimming the screen when you enter a dark room [3];
- Throttling the processor's clock speed when it gets too hot [4];
- Shutting the phone down when water is detected inside the phone;
- Feed data from accelerometers and gyroscopes through to running applications [5, 6];
- Turning the touchscreen off when the proximity sensor detects the phone near your ear.

The proximity sensor is the focus of this thesis. It needs to be as small as possible, as there is limited available space inside phones. Several types of solutions exist for this problem, such as position sensing devices, ultrasone sensors, and intensity sensors. However, when selecting a method, the environmental effects should be taken into account. Photons in the near-infrared dissipate after a limited distance. One of the conclusions of section 3.1 is that after only a few meters, from a light source emitting 5 mW, only a few hundreds of photons per second return to this light source. Sound can propagate much further. Studies have shown that orcas in the ocean are negatively affected by boats on the surface [7], as well as animals and children [8]. Moreover, the atmosphere absorbs photons as well. This is not noticeable after a few meters, but after a certain distance, there are no photons left. The following animals are sensitive to infrared light:

- Several types of snakes can see in the far-infrared;
- Mosquitos and bedbugs use purely infrared vision to feed themselves;
- Some types of frogs and fish can generate an enzyme that enables infrared vision depending on their environment.

A system with a laser operating in the infrared region will influence these animals. How frogs and fish truly see the laser, none can tell. European guidelines stipulate a maximum power consumption of 5 mW [9], products adhering to this norm should not hurt animals. Furthermore, in the use case of proximity sensing in phones, the device should not be on permanently but only periodically.

To summarize, certain animals may be affected by the device, but it will not harm them.

Measuring the time of flight of light is a relatively new solution to the problem of distance measurement. Here, the distance and time are related via the speed of light. The travel time of light can be measured with a source of light, a single-photon detector, and an accurate time measurement device. This travel time is related to the distance between sensor and target via the speed of light. A schematic of such a system is shown in fig. 1.1.

This technology presents two main problems: detecting single photons and measuring the round trip time of this photon accurately enough. The former is solved by single-photon avalanche diodes (SPADs). A SPAD is an NP-junction that is put into breakdown mode. An arriving photon that hits the device creates an electron-hole pair in the depletion layer. Because of the high voltage, these electrons will generate more electron-hole pairs, resulting in a high current. This high current, which is created

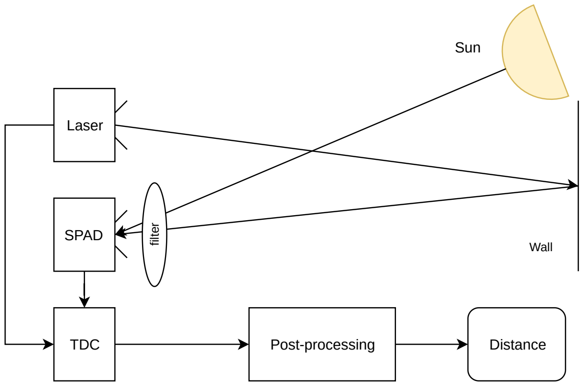

Figure 1.1: Basic system setup. Photons from the laser bounce off the wall and return to the SPAD. Photons from the sun that are not filtered by the optical filter hit the SPAD as well. The SPAD emits a pulse which is converted to time by a time-to-digital converter (TDC). The distance is recovered by a processing algorithm.

within an extremely short time interval, is called an avalanche.

The second problem is detecting this current with the required resolution. If a resolution of 1 mm is required, this translates to a time interval of 6 ps. While transistors are fast and getting faster, this is beyond the capabilities of counters in many silicon processes. Furthermore, even if a fast enough counter could be manufactured, power consumption in this counter is enormous, as the required switching intensity is given by [10]:

$$I_{\text{switching}} \sim \frac{f \cdot C \cdot V^2}{A_{\text{transistor}}} \tag{1.1}$$

Given a frequency of 100 GHz, translating to 10 ps resolution (1.5 mm), a capacitance in the order of 1×10^{-16} F [11], and a voltage of around 1 V, the switching intensity would be in the order of several mW/µm^2 [10]. The required switching speed is also only available on small, sub-60 nm nodes, which are costly to use. Alternative time measurement solutions need to be found instead.

This thesis answers the following questions regarding proximity sensing using time-of-flight:

1 **What are trade-offs found in current state of the art proximity sensing devices?**

2 **In what area does time of flight technology shine?**

3 **What are the typical worst-case signal and noise conditions for such a system?**

4 **How well does such a system perform, what is the standard deviation of the measurement?**

The thesis is organized as follows. First, the current state of the art is analyzed in chapter 2. Different proximity sensing methods are compared, and a product analysis is performed. The physics of SPADs are reviewed and TDC architectures are compared. Chapter 3 analyzes an algorithm to recover distance from the arrival times of single photons. Arrival rates of photons due to laser and ambient light are calculated, and a formula is found that produces the expected standard deviation of a measurement. In chapter 4, several simulators are created that verify the found formula. Lastly, the work is concluded in chapter 5, where answers to all research questions are summarized.

2 Background

Proximity sensing in phones is not a recent problem. It has been solved many times already. When the distance sensing should be independent of reflection, however, several techniques are unavailable. When on top of this, short distances need to be measured, and the sensor should consist of one part and be as small as possible, time of flight is a clear winner. This chapter will discuss the different proximity sensing techniques available, as well as why some of them are unavailable in our circumstances, leading to the choice of time of flight with SPADs.

First, different techniques are discussed to obtain distance digitally. Secondly, a product and patent analysis is performed to see what products already exist. Based on the target application and the found products, a combination of parameters is found where a new product might be able to improve. After validating the choice of direct time of flight (dToF) technology using SPADs, deeper research into the physics of SPADs, TDCs and lasers is analyzed. Lastly, because of the extreme constraints, implementation details for TDCs on FPGAs are discussed

2.1. Solving the distance measurement problem

As said, many solutions exist for the problem of distance measurement. A simple method is intensity-based:

2.1.1. Intensity

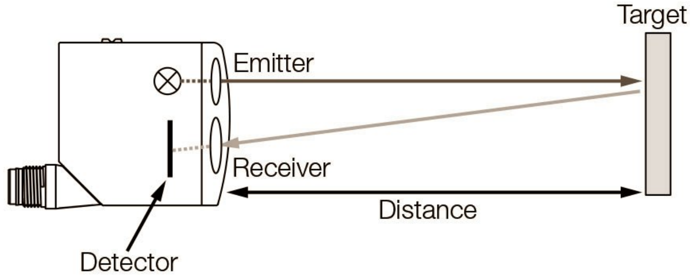

Figure 2.1: Working principle of intensity-based proximity sensing. Light is emitted by the device. A fraction of the light reflects off of the target and arrives at the receiver. The intensity of the light hitting the detector is a quadratic measure for the distance [12].

This technique can be used with infrared LEDs, where a pulse is sent out and the intensity of the returned pulse is observed. However, this is unreliable when working with different materials because of absorption and reflection gradients of different materials. Furthermore, ambient light will introduce a measurement error linearly related to the intensity of the light.

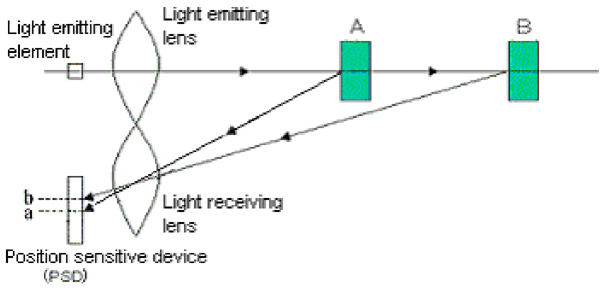

Figure 2.2: Working principle of PSD-based proximity sensing. Light is emitted and bounces off of a target. It hits the receiving lens in a point. The angle of the light in this point is a measure for the distance of the target [13].

2.1.2. Position sensitive devices (PSDs)

A position-sensing device works by measuring the angle of return. An example is shown in fig. 2.2. The technique is fast, since the pulse travels at the speed of light, like photon time of flight. The resolution is typically excellent, up to 0.01 μm [14]. However, with dark objects, the resolution goes down significantly because of a lack of reflected light [14].

Advantages

- High resolution;
- High refresh rate;
- Low-power.

Disadvantages

- Dark object reduce resolution;
- Light-emitting element and PSD need to be separate.

2.1.3. (Ultra)sound time-of-flight

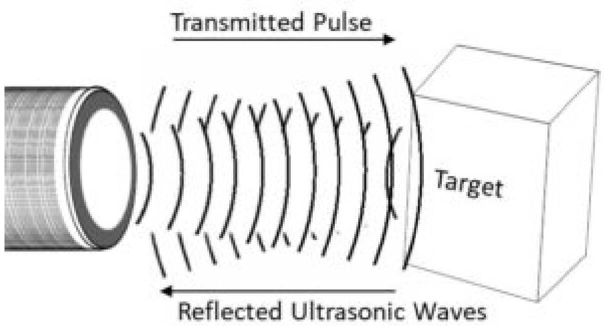

Figure 2.3: Working principle of ultrasound-based proximity sensing. A series of chirps are emitted by the device. These waves reflect off of the target and arrive at the detector after some time. The time is linearly related to the distance via the speed of sound [15].

Instead of an electromagnetic wave, this method uses ultrasound waves that bounce off of the target. This is a low-power technique [16] but it is also severely limited because of its slow travel (only at the speed of sound). This means the refresh rate is limited at high ranges. Furthermore, because of coupling the minimum distance that can be sensed accurately is also limited. Also, ultrasonic pulses reflect less well off of soft targets like clothing or animals [17].

Advantages

- High resolution achievable;
- Low-power [16].

Disadvantages

- Refresh rate low because of wave travel at speed of sound;
- Minimum distance relatively high because of ringing effects;
- Sound travels far into the environment which may have negative effects.

2.1.4. (In)direct light time-of-flight

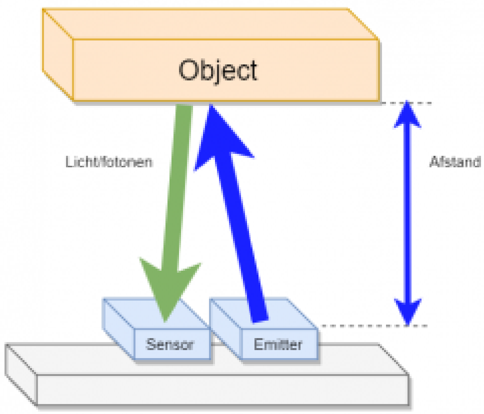

Figure 2.4: Working principle of ToF-based proximity sensing. A fraction of the emitted light is reflected by the target and hits the sensor. The time between photon emission and arrival is measured with high precision. This travel time is linearly related to the target distance [18].

This is the main focus of this thesis. Using this technology, a pulse is sent out, reflects off of a target, and returns. The time that the pulse takes to do this is indicative of the distance to the target. When done with light, a high update rate can be achieved, since pulses travel so quickly. Achieving high resolution is more difficult since this translates to extremely small time intervals [19].

Advantages

- Low-power;
- Whole sensor in 1 package, can be integrated with laser [19];
- High refresh rate;

Disadvantages

- Achieving high resolution requires typically difficult high-resolution time measurements;
- Returned light fraction drops quickly, performs less well in highly ambient environments.

2.1.5. Product comparison

State of the art sensors using different technologies are compared in table 2.1. In this table, some information is missing. Not all datasheets include all information that is relevant for this product study. However, the found products still give a good overview of what is possible using different technologies.

From most manufacturers, only a few products are listed. Typically, more products exist. For conciseness, only the most extreme products are displayed, i.e. the one with the highest resolution and the one with the lowest power usage out of a product range.

While datasheets contain lots of information, only the properties that are indicative of performance and efficiency are selected. Physical size, interfacing, and similar aspects are ignored. When considering the use of a product in this direction, usually the former aspects are much more important, as the product can be changed to accommodate the latter aspects of the selected device.

2.1.6. Conclusion on proximity sensing methods

The analysis above corresponds to the product analysis in table 2.1. The most low-power products are the single-package ICs from ST [20, 21]. The products with highest range are also time of flight based [22], but the highest resolution is obtained by PSDs [23]. The existing ultrasone devices perform badly below a few centimeters, because of ringing.

For phones, the most important aspects are power consumption, an okay resolution and a range from zero to about half a meter. Furthermore, PSDs cannot be used because the light emitting part and the detecting part have to be placed together, a phone has no space for a different solution. Because of this, time of flight with light is what will be used in the remainder of this thesis.

Time of flight with light requires a light emitter and a light receiver. The former will be discussed in section 2.2 and the latter afterwards in section 2.3.

2.2. Lasers

Many sources of light exist. However, not many fulfill the requirements imposed by time of flight:

- Low switching time;
- High efficiency;
- Small form factor;
- Integrated with CMOS package.

Because of these requirements, the only suitable devices are lasers, VCSELs and LEDs. Lasers are available at several wavelengths. The most popular are 850 nm and 940 nm [46]. Intuitively, a wavelength should be chosen that is relatively empty, in the sense that there are few other sources in the natural environment. The 940 nm wavelength is more suitable, because Earth's atmosphere absorbs light at this wavelength. This is discussed in more detail in section 3.1.2.

Lasers operating at this wavelength are commercially available and can be integrated in the same package as a chip. This thesis focuses on what these lasers can be used for. The challenges in laser design are left out of scope.

2.3. Single-Photon Avalanche Diodes (SPADs)

This section will answer the questions what a SPAD is, what it is used for and explain its typical operating behavior. First, a brief overview of SPAD physics will be presented, followed by typical operating behaviour and effects that should be taken into account. The most important effect, saturation, will be discussed separately because of its importance.

2.3.1. Overview of SPAD physics

A SPAD is a p-n junction biased above breakdown [47]. It is equipped with avalanche quenching and rebiasing peripheral circuits. Figure 2.5 shows typical behavior of a diode and a SPAD.

Looking at fig. 2.5b, showing the I-V curve for a typical p-n junction, three main regions are identified: Breakdown, reverse and forward mode. For typical diodes, forward and reverse mode are the only used operation modes [49]. However, a SPADs function on the edge between reverse and breakdown mode. Breakdown occurs when accelerated carriers cause electrons to move. Breakdown can be subdivided into the Geiger-mode and the linear region. In the latter case, the gain per injected electron is expected to be linear. In Geiger-mode, however, the current will continue to rise. To be in Geiger-mode, the expected number of created carriers per carrier must exceed one. Every charge injection will then lead to an avalanche. The voltage required to meet this condition is called the breakdown voltage. If a higher voltage than the breakdown voltage is applied, the remainder is called the excess bias. One example of a charge injection could be due to a single photon, which is absorbed by electrons in the silicon, removing these electrons from the grid. Because of the voltage, these now-free electrons will travel at high speed and free more electrons. This is where the SPAD gets the name.

If the SPAD is operating continuously in avalanche mode, the large power consumption will destroy the SPAD. However, a SPAD placed in series with a large resistance, as shown in fig. 2.5a, exhibits different behaviour. A starting avalanche current will lead to a high current through the resistor, quenching the avalanche as it is starting. As the excess bias voltage is reduced to zero (*quenching*), the amplification factor of the SPAD will drop and the current will drop as well, causing the excess bias to rise again (*re-biasing*). This process is shown in fig. 2.5d and fig. 2.5c. Because the time of maximum avalanche current is now limited to nanoseconds, overheating is less of an issue [47]. However, with

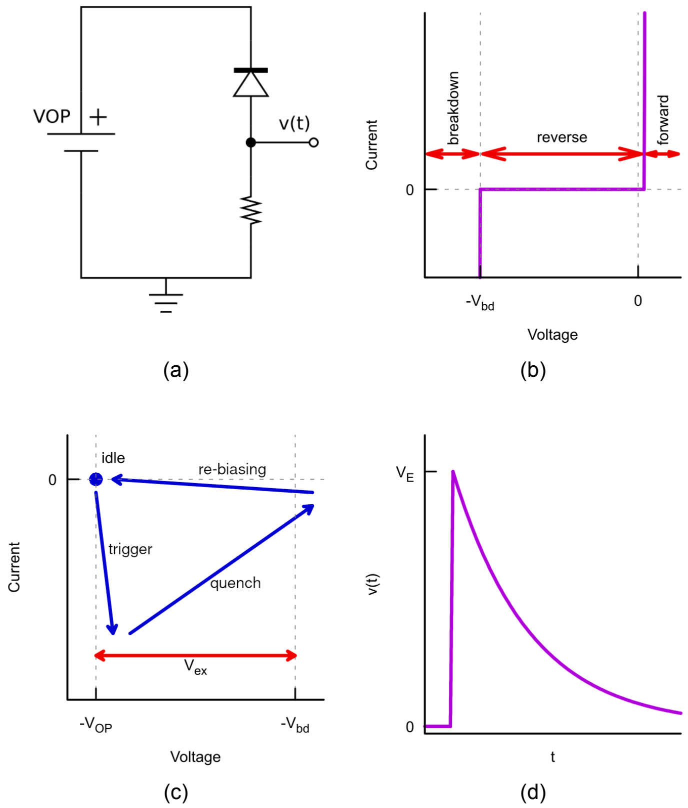

Figure 2.5: SPAD circuit and operation. a) shows the simplest SPAD circuit for single-photon detection, b) the I-V characteristic of the SPAD and its operating regimes, c) its operating points and d) the output voltage during one detection (Adapted from [47, 48])

passive quenching, the trigger-quench-rebias cycle is slow. Active quenching can improve the speed of this cycle significantly, bringing the average dead time of the SPAD to 5 ns to 7 ns [50–54]. In 2003, SPADs with a dead time of 50 ns were already reported [55]. Additionally, the quenching method affects the behavior of the SPAD when a charge hits while the SPAD is considered dead, i.e. in quenching or re-biasing mode. This is elaborated upon in section 2.3.5.

2.3.2. Probability of photon detection

For a photon to be detected, several conditions must be satisfied. First, the photon should enter the silicon and not be reflected at the device surface [56]. Second, the photon must be absorbed to generate an electron-hole pair. Lastly, the generated charge carriers should generate an avalanche. The probability of these conditions being satisfied per photon depends on the wavelength of the photons, as shown in fig. 2.6 [56].

At 1100 nm, silicon is translucent. Photons with a wavelength higher than this cannot be detected by silicon. As the wavelength of a photon approaches this boundary, the photons get increasingly difficult to detect. This is illustrated in fig. 2.7. While in SPAD design, some parameters can be adjusted to correct for poor photon detection probability in near infrared, a SPAD is fundamentally worse at detecting photons at wavelengths near 1100 nm than it is at detecting 400 nm to 500 nm photons.

2.3.3. Noise sources in SPADs

Single photons are one source of carrier injections which will lead to an avalanche. So-called false counts can occur due to several phenomena.

Dark count rate

The dark count rate, comparable to dark current in photodiodes, is the detection rate due to carriers not induced by photon absorption [56]. These false counts are introduced by thermal generation and

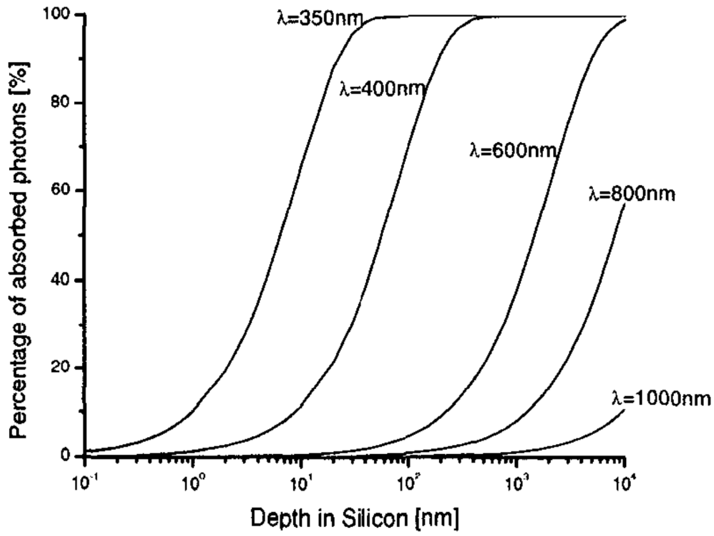

Figure 2.6: Theoretical photon detection probability as a function of silicon depth for different photon wavelengths [56]

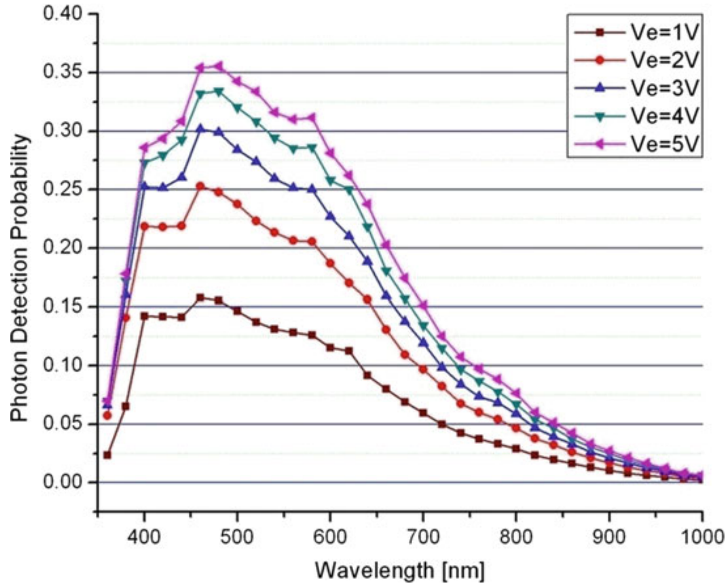

Figure 2.7: Photon detection probability in a SPAD implemented in 130 nm CMOS process as a function of wavelength for different excess bias voltages [47]

band-to-band tunneling. For a mathematical analysis, see [56]. It suffices to say that the dark count rate depends on temperature, excess bias voltage, and impurities during fabrication. For a number of SPADs, the DCR is shown in fig. 2.8.

Afterpulsing

During an avalanche, many carriers travel through the depletion region. Some of them may become trapped in the band gap between the conduction and the valence band. These are released after some time. If they are released after the SPAD is rebiased, one of these trapped carriers could trigger an avalanche again. This pulse is called an afterpulse [57]. The probability of an afterpulse occurring is highly dependent on temperature [47] and also on the dead time [58]. The time between a trigger and an afterpulse from this trigger can vary, as seen in fig. 2.9. Afterpulsing causes counts that do not conform to the Poisson distribution, thus changing the distribution of counted photons.

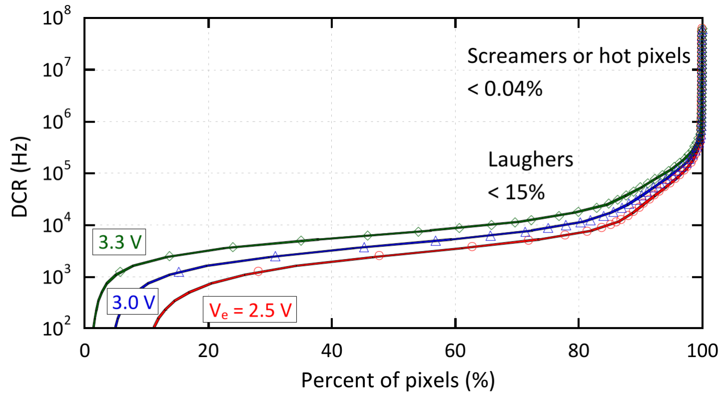

Figure 2.8: Cumulative DCR as a function of SPADs population for different excess bias voltages. Most SPADs have a DCR in the thousands [48].

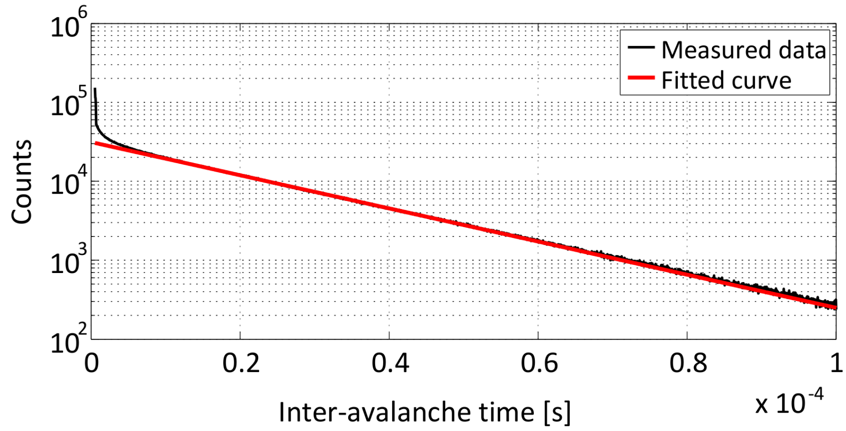

Figure 2.9: Histogram of time between two avalanches due to afterpulsing. The afterpulse is most likely to occur within microseconds, but maybe delayed by tens or hundreds of microseconds [48].

Electrical and optical crosstalk
Afterpulsing is not the only source of noise correlated with arriving photons. Recombining electron-hole combinations during an avalanche may generate more photons, creating optical crosstalk with other SPADs close by [52]. This can be partially prevented by isolating the SPADs. Electrical crosstalk can also happen, when high-energy carriers exiting the depletion region of one SPAD are injected into the depletion region of another SPAD [47].

2.3.4. SPAD rebiasing mechanisms

The simplest recharge mechanism is a passive resistor in series with the SPAD, as shown in fig. 2.5a. However, it is slow and prone to afterpulsing, and other recharge mechanisms have been devised as a result. However, more complicated circuits use die area that could have been detecting photons. A trade-off is observed, where the peripheral quench- and re-bias circuits should be as small as possible to keep the active area as large as possible, but also reduce afterpulsing as much as possible.

As shown in fig. 2.10, rebiasing can be done in different ways, each leading to a different afterpulsing probabilities and dead times. Furthermore, the effect of a photon during the dead time is different. The first graph shows a passive resistor, which gives an exponential drop in voltage over the resistor as the current through the resistor decreases. The excess bias voltage is restored almost immediately. The second graph shows a slightly more complicated circuit including one transistor. The excess bias voltage is now restored linearly after the SPAD is dead for a short while. This gives the SPAD more time to flush hot carriers, reducing the chances of an afterpulse. In the third graph, this is shown to an extreme. The SPAD stays near breakdown voltage for a relatively long time and is rebiased quickly. This circuit requires more area, but the change in behavior is more fundamental than an afterpulse probability reduction. Because the SPAD is operating near breakdown voltage for so long, photons

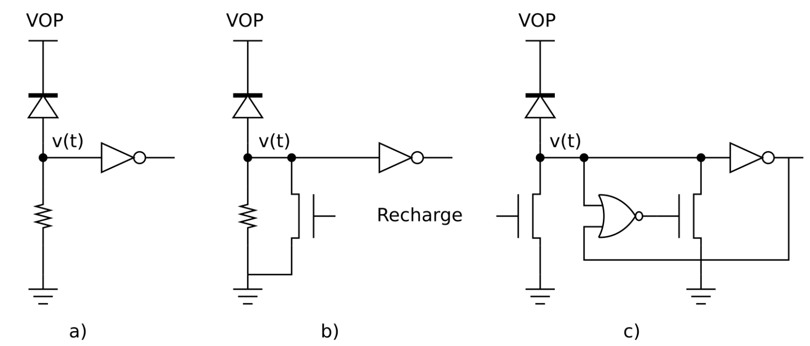

Figure 2.10: Different SPAD quenching and recharge implementations. Passive quenching stops the avalanche. In circuit a), recharging is passive. In b), a single-slope active recharge and in c) a dual-slope active recharge rebiases the SPAD [48].

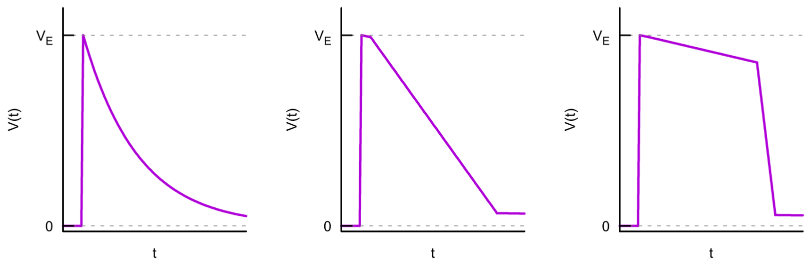

Figure 2.11: Different `v(t)` as shown in fig. 2.10 with different rebiasing circuits. Trapped charges in the SPAD which relax after a fixed time are more likely to trigger another avalanche in the first and second circuit, as the SPAD is rebiased quickly. However, this increased resistance to afterpulsing is a trade-off with a more complex rebiasing circuit [48].

hitting during dead time do not contribute to another avalanche. How does that relate to SPAD behavior in high photon rate conditions, when the probability of a photon hitting during dead time is higher?

2.3.5. Photon overflow: paralyzing and non-paralyzing rebiasing mechanisms

Photon arrival events on a SPAD without dead time follow Poisson statistics [59]. However, a long dead time introduces non-Poisson features in the observed counting rate and variance of arrival times of photons [60]. Two simple ways of explaining these deviations are the non-paralyzable model and the paralyzable model [60]. A new simulation method is proposed that supports both paralyzable and non-paralyzable models, as well as a hybrid combination of the two. This can be seen in fig. 2.12.

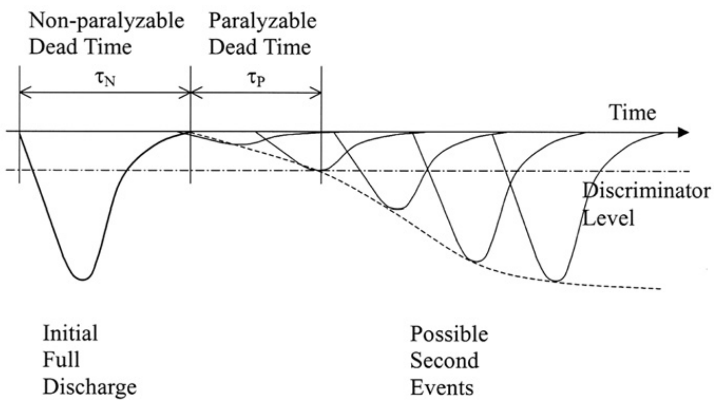

Figure 2.12: Dead time behavior during non-paralyzable and paralyzable-time. Photons arriving after during the start of the paralyzable dead time lead to paralysis, an extended dead time but no extra detections [60]

The type of quenching circuit can be determined at system design time and is not dependent on the SPAD. For the application described in this thesis, the active area of the design is irrelevant. Only imaging sensors choose passive quenching circuits because then the SPAD is a larger part of the total design, leading to better resolution given a fixed area. For distance sensing, this is less of an issue, from now on the assumption is made that a good active quenching circuit is available.

2.4. Time-to-Digital Converters (TDCs)

Now that a device is known that can detect single photons, a read-out method is needed that can determine the exact time of arrival of these photons. The required resolution must be high; to distinguish 1 mm of distance, the resolution of the TDC should be less than 6 ps. For some (large) technologies such as 180 nm CMOS, the switching time of single transistors is in the order of 10 ps to 100 ps depending on fan-out.

2.4.1. Time discretization techniques

Before any time discretization techniques can be discussed, performance metrics are needed. Some metrics are [61, p. 70]:

- *Resolution:* The range of input values represented by the same output code;
- *Area:* The occupied silicon area;
- *Energy:* The energy consumed for a single conversion;
- *Speed:* The number of times that can be discretized per second;
- *Dynamic range:* The ratio between the largest and smallest input values that are accepted;
- *Integral nonlinearity (INL):* The deviation of of the transfer function from a line, expressed in LSB;
- *Differential nonlinearity (DNL):* The derivative of the INL;
- *Gain error:* The ratio between average transfer gain and desired gain;
- *Offset:* The average difference between the input and output times;
- *Single-shot precision (SSP):* The variance of the output code when the same input is applied, expressed in LSB.

Using these criteria, different methods for time discretization can be discussed.

Simple counters

The simplest time discretization technique is a counter. A counter consists of n bits and can count from 0 to $2^n - 1$. As transistors get smaller and the switch time of a single gate becomes lower the achievable resolution increases. Using 64 or even 128-bit counters, the dynamic range is practically unlimited. Power usage scales with $\mathcal{O}(2^{n+1})$, as the LSB flips once for every least significant bit. The area consumed is low compared to other architectures, described below. Only an n-bit incrementer with n flip-flops are required.

Flash TDC

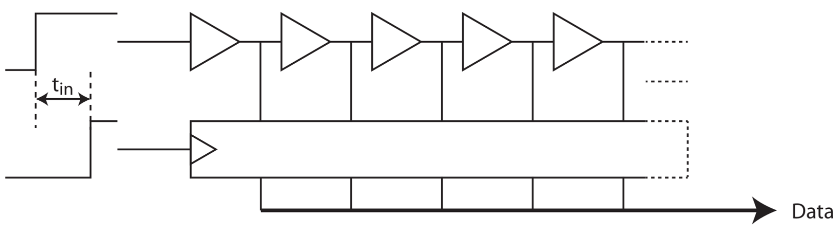

Figure 2.13: Simplified schematic of a flash TDC [61].

A flash TDC, comparable to a flash ADC consists of a delay line and a set of flipflops. The time difference input arrives as the switch time of two input lines. It is shown in fig. 2.13. A start pulse is fed to the delay line. When the stop pulse arrives, all flipflops will store the current state of the delay line. This structure is much more expensive in terms of area because to count from 0 to N takes $2N$ flipflops. Furthermore, mismatch between the delay elements means an increasing uncertainty accumulates throughout the chain. This is the limiting factor of the length of the line. The readout time is one cycle of a flip-flop. The energy consumption is much higher than that of a counter. The energy consumed per sample is at least that of one toggling delay element and one flip-flop.

Ring delay lines

As seen above, a line is suboptimal because it requires a large area and the mismatch between elements accumulates throughout the line. Both of these problems can be solved by integrating a partial counter into the ring. The mismatch is now observed in the form of a cyclic linearity error. Power consumption is approximately equal to the flash TDC, though the required area is much less. The readout time is equal to the readout time of the flash TDC.

However, the resolution is still limited to one delay element. A better resolution can be obtained with a vernier line.

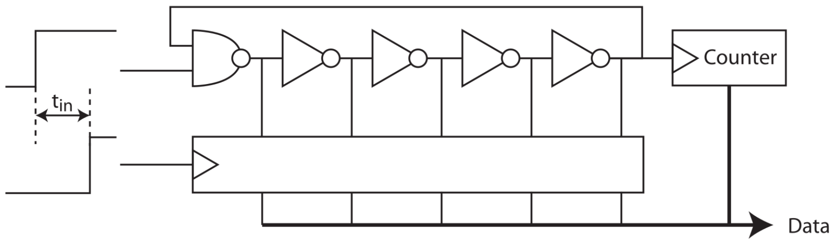

Figure 2.14: Simplified schematic of a ring TDC [61].

Vernier delay line

To get a resolution of less than one delay element, the difference between a delay element and another slightly smaller delay element can be used. An example of such a delay line is shown in fig. 2.15. The start pulse goes into the slower delay line, the stop pulse into the faster one. Arbiters (indicated with an A) determine which signal arrives first. The first arbiter where the stop pulse arrives earlier than the start pulse gives the time difference.

This TDC is limited by the matching between elements, as the difference between the delay elements needs to remain sufficiently constant throughout the delay line. The area of this vernier line is at least twice as large as the flash TDC, and the power consumption is as well.

Furthermore, in this TDC resolution is traded for readout time. Both pulses need to travel through the entire delay line, where the delay difference is smaller than the delay of the individual elements. On top of this, arbiters are usually slow. The sampling rate is thus limited.

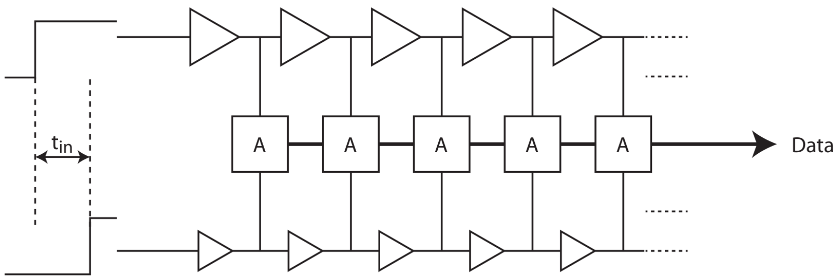

Figure 2.15: Simplified schematic of a Vernier delay line [61].

Vernier ring

Like the flash TDC, the vernier line can be converted into loop-form, as shown in fig. 2.16 where five vernier elements are used. A counter is added to count the number of completed loops. The arbiters need to be quick enough to complete and reset before the ring loops around.

Power consumption is slightly better than the vernier line, as the bottom ring is only active once the stop pulse has been received. However, it is still high. Furthermore, to be useful, the ring needs to consist of many elements.

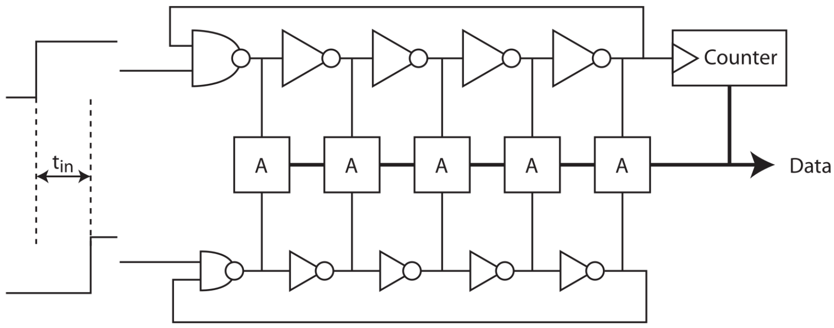

Figure 2.16: Simplified schematic of a Vernier ring [61].

Pulse-shrinking
Pulse shrinking is a fundamentally different technique. The time input does not arrive as two pulses rising with a time delay, but as one pulse where the time input is the width of the pulse. Delay elements are used that have different propagation delays for rising and falling edges. The position of the element where the pulse width reaches zero is a measure for the time input. An example is shown in fig. 2.17.

The energy consumption is much lower than the vernier line, as only 1 line is used. Furthermore, there is no need for a reset procedure as the line will be reset to zero after the conversion. However, the linearity depends on a matched difference in propagation delay between rising and falling edges.

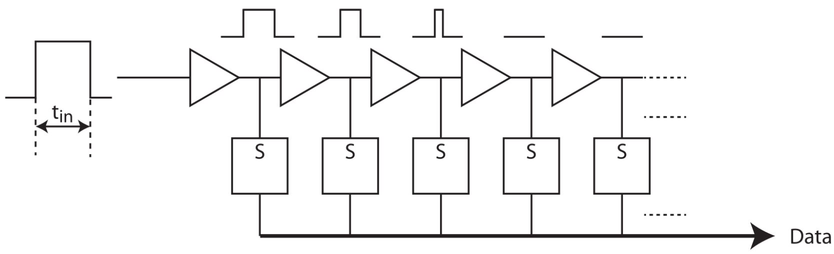

Figure 2.17: Simplified schematic of a pulse-shrinking TDC [61].

Successive approximation
A successive approximation TDC is a fundamentally different method of measuring time differences. A binary search is executed to align both edges. Every cycle, an arbiter determines which edge is faster, and this edge is delayed by half the time-scale. In the next round, the delay is halved. An example is shown in fig. 2.18.

Successive approximation register (SAR) TDCs are slower than flash TDCs, but the delays are grouped. This may be advantageous in implementation. While arbiters decide which edge is first, both lines need to be delayed, which means the sampling rate is limited and the readout time is high.

Combining TDCs
Instead of choosing only one TDC, multiple TDCs can be combined. This is already the case for the flash ring and vernier ring architectures. A coarse counter is used to reduce the space overhead of the TDC.

The architectures above show that achieving sub-delay resolution requires area, time and energy. If the necessity to achieve this resolution can be circumvented, the TDC would be much simpler to implement.

However, if high resolution is necessary, then a coarse counter in combination with a fine-grained TDC is useful. The power-hungry fine-grained TDC is on for a small portion of the time.

2.4.2. Product analysis
Next to a theoretical analysis, products were analyzed as well. They are shown in section 2.4.2. Note that these are discrete TDCs, and the performance is thus worse than if the TDC is included on-chip. For a comparison including TDCs from papers, see [61, p. 18].

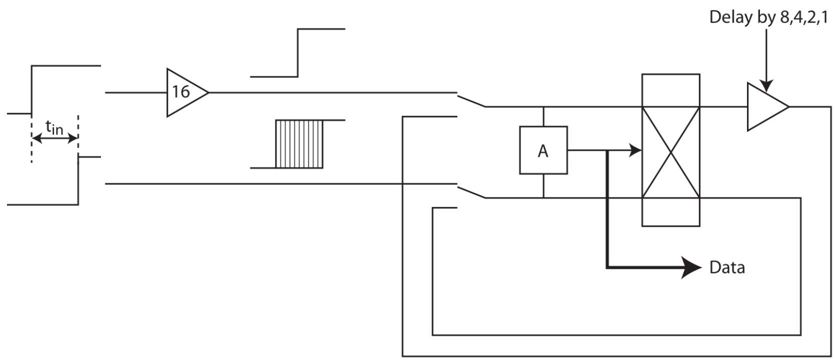

Figure 2.18: Simplified schematic of a SAR TDC [61].

Product	Technique	Range (μs)	Res (ps)	ToF freq	Power (W)	Channels
MAX35101 [62]		8000	20	64		2
AS6501 [63]		1.6×10^7	20	3.5×10^7	0.26	2
TDC-GPX2 [64]		1.6×10^7	20	3.5×10^7	0.45	4
TI TDC7201 [65]	Ring Osc	12 ns to 2000 ns	55		0.014	2
TI TDC7201 [65]	Ring Osc	500 ns to 8×10^6 ns	55		0.014	2
TDC-GP22 [66]		500 ns to 4×10^6 ns	90	1×10^6	0.012	4

Table 2.2: Comparison of Time-to-Digital converter ICs

It can be seen that a high resolution can be obtained of up to 20 ps (3.5mm). There is also a large gap in power consumption, some chips consume over 10 times as much power as others.

The time range where signals can be received varies wildly, from nanoseconds to seconds. Distinguishing time measurement techniques is much more difficult because except for TI, most manufacturers don't specify this. However, a lot of documentation already exists regarding this [61].

All of the sensors have at least two channels, this is because the start and stop pulse arrive separately. Usually, it is difficult to determine within a few picoseconds when exactly the laser fires. Thus, the timer is started before the command to fire the laser is sent, then the signal from the laser arrives first to the SPAD, followed by the signal reflected by the object. This method needs at least 2 channels to be available.

2.4.3. Conclusion on architectures of TDCs

Many TDCs architectures exist. While the best one depends on the use-case, it seems a combination of a counter with a flash TDC is a good option if sub-delay resolution needs to be achieved. Using a Johnson counter [67] in combination with a coarse counter yields good resolution while energy usage and area usage are limited.

Product	Name	Underlying technique	Range (m)	Res (m)	Refresh (Hz)	Power (W)	λ (nm) / f (Hz)	Notes
ST VL6180X [21]	FlightSense ToF	SPAD dToF	0 to 0.1	0.002		0.005	850 nm	Light < 1 klx to 100 klx
ST VL53L1X [20]	FlightSense ToF	SPAD dToF	0 to 4	0.02	50	0.02	940 nm	Light < 200 kcpSPAD
TeraRanger One [24]	IR ToF	iToF	0 to 14	0.005	600 to 1000	0.6		4 cm accuracy
TeraRanger Evo 600Hz [25]	IR ToF	iToF	0.75 to 8	0.005	600	1		Accuracy of 12 cm
TeraRanger Evo 3m [26]	IR ToF	iToF	0.1 to 3	0.005	100	1.3		-
TeraRanger Evo 60m [27]	IR ToF	iToF	0.5 to 60	0.02	240	1.7		-
Benewake TF Mini [28]	IR ToF	iToF	0.3 to 12	0.005	100	0.12	850 nm	> 100 klx, 3 m max
Garmin LIDAR v3HP [29]	LiDAR	iToF	1 to 40	0.01		1.7	905 nm	Expensive ($150)
LeddarVu [30]	solid stage LiDAR	iToF	0 to 165	0.05	100	2	905 nm	-
Seeedstudio Grove [31]	LiDAR	iToF	0.3 to 12	0.005	100	0.12	850	< 70 klx
RPLIDAR A3M1 360 [32]	LiDAR	iToF	0 to 25		20	3	785 nm	-
SensorPartners LAM 5X [33]	Laser distance measurement	iToF	0.1 to 150	0.003	10	3.2	650 nm	Uses 26 W for heating; Explosion-proof
Scantron SLS [34]	Phase shift distance sensor	iToF	0.1 to > 30	0.003	5	1.5	650 nm	Measure phase
AFBR-S50MV85G [35]	Motion measurement sensor	ToF	0.01 to 10	0.005	3000	0.18	850 nm	< 200 klx
Simblee RFD77402 [36]	IoT 3D ToF	ToF	0.1 to 2	10 %	10	0.05	850 nm	Dark env, 90 % reflect.
ISL29501 [37]	ToF DSP	APD iToF	0 to 33.3			0.2	N/A	Diode not included
Baumer OM70 [23]	Laser distance sensor	IR PSD	0.03 to 0.07	0.7 µm	1540	2.85	660 nm	Light < 28 klx
Sharp GP2Y0A21YK [38]	Analog Distance Measurement	IR PSD	0.1 to 0.8	N/A		0.2	850 nm	-
Sensopart FR 90 ILA [22]	Reflector distance measuring device	IR PSD & ToF	0.5 to 250	0.0001		3	905 nm& 650 nm	PSD < 2 m; ToF > 2 m;
Sensopart FR 55 RLAP [39]	Reflector distance measuring device	IR PSD & ToF	0.3 to 70	0.0004		0.9	655 nm	PSD < 2 m; ToF > 2 m; < 20 klx
MLX75024 [40]	Optical ToF	Depthsense ToF					850 nm & 940 nm	Binning: < 210 klx
Baumer OADM [41]	Optical Distance Sensor	Optical Add Drop Mux	0.2 to 13	0.005	100	3	660 nm	Light < 40 klx
Baumer U500-DA0.2 [42]	Pulse Echo	Ultrasone	0.07 to 1	0.0003		2.85	200 kHz	-
Maxbotix HRLV MB1043 [43]	Ultrasonic Rangefinder	Ultrasone	0.03 to 5	0.001		0.024		-
Sensopart UM 18-60 [44]	Ultrasonic Proximity Switch	Ultrasone	0.03 to 0.25	0.0036		0.9	320 kHz	-
Sensopart UMT 30-3400 [45]	Ultrasonic sensor	Ultrasone	0.35 to 3.4	0.18		2.4	120 kHz	-

Table 2.1: Proximity sensing equipment comparison. Sorted by technique, then resolution, then range. dToF: direct Time-of-Flight. iToF: indirect Time-of-Flight. IR: Infrared. PSD: Position-sensing device. APD: Avalanche photodiode.

3

Mathematical analysis

Now that sufficient background knowledge is established a potential system, shown in fig. 3.1, will be analyzed. The system is based on the time-of-flight principle and consists of:

- At least one SPAD;
- A readout circuit that can measure the time of photon arrival with high resolution;
- A laser capable of high-frequency pulsing, at a wavelength of 940 nm;
- An optical filter on top of the SPAD, constraining light arrival to the 920 nm to 960 nm range;
- Hardware to implement the proposed algorithm; it should reject noise from sunlight and measure the time delay between transmission and reception of laser photons.

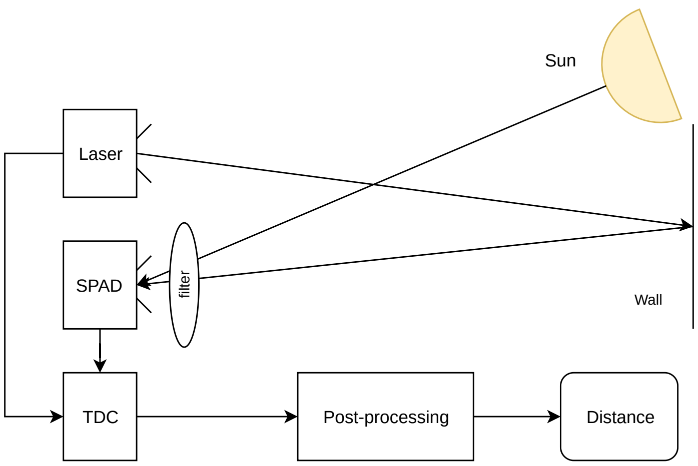

Figure 3.1: Basic system setup. Photons from the laser bounce of the wall and return to the SPAD. Photons from the sun that are not filtered by the optical filter hit the SPAD as well. The SPAD emits a pulse which is converted to a time by the TDC. The distance is recovered by a processing algorithm.

First, (average) photon arrival rates from the laser and the sun are calculated in section 3.1. The variance of these rates is discussed in section 3.2, specifically when the SPAD approaches saturation. Next, a recovery algorithm is proposed and analyzed in section 3.3. This results in a formula for the standard error. Because this formula is found to be independent of the resolution of the TDC, the effect on the standard error of lowering the resolution is studied in section 3.6. The effect of using multiple SPADs is analysed in section 3.4. Lastly, the effect of the waveform emitted by the laser is analyzed in section 3.5.

3.1. Average photon arrival rates

How many photons hit the SPAD per second due to the laser or noise? This is given by the sum of its parts:

$$R_{\text{total}} = R_{\text{laser}} + R_{\text{noise}} \tag{3.1}$$

This section quantifies these rates. It is important to realise that this is the average photon rate, over a large period. The actual amount of photons observed will vary. This variation is discussed in section 3.2. For now, one way to view the calculation result is the average amount of photons per second when observing photons for a large time.

3.1.1. Photon rate due to laser

The returned signal power depends on many factors. The photon return rate from the laser to the SPAD via a target can only be solved if assumptions about the environment are made. First, a scenario will be defined, including all assumptions. Then, a rate is calculated given these assumptions and constraints.

Conditions for calculating photon arrival rate due to laser

The field of view, or opening angle, of the laser and the SPAD are assumed equal. It is also assumed that the target object is at least as large as the field of view, and exactly perpendicular to the center of the SPAD field of view. These assumptions will not always hold, of course. However, they do provide a baseline for what performance can be achieved.

All photons emitted by the laser arrive at the target. Depending on the reflectivity χ_{R} of the target, photons are reflected. Reflectivity depends on many properties of the target material. This is elaborated upon in appendix B. Due to the many folds and forms in human skin, as well as clothing, determining reflectivity accurately is not possible. Because of this, the average reflectivity of human skin will be used. For skin types I and II on the Fitzpatrick phototyping scale, reflectivity at 940 nm is about 0.53. For skin types III and IV, $\chi_{\text{r}} \approx 0.45$, and for skin types V and VI, $\chi_{\text{R}} \approx 0.36$. Based on this, $\chi_{\text{R}} \approx 0.4$ is taken as a good enough approximation of all humans [68, 69].

Signal rate for an infinitesimal field of view

Assuming that the field of view is small, the light will travel from the laser to the wall and arrive at a point (1). At this point, the wall will absorb some light, and the rest will reflect in a hemisphere according to Lambert's cosine law [70, p. 13]. The reflection of light is shown in fig. 3.2. The opening angle of

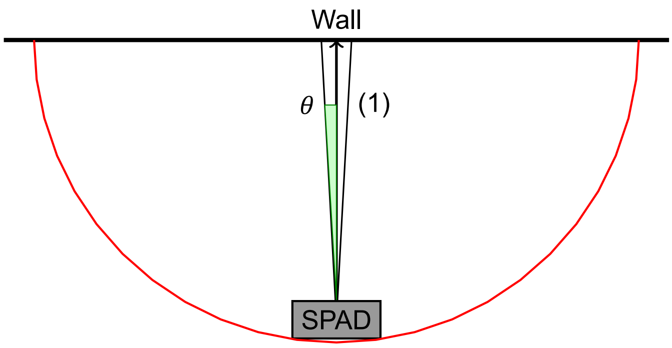

Figure 3.2: Laser light hitting a wall and returning in a hemisphere. The fraction of light that returns to the SPAD is equal to the area of the SPAD, divided by the area of the hemisphere which is just as far away as the SPAD is.

the laser, which is equal to the opening angle of the SPAD, is defined as θ. The returned photon rate shown in fig. 3.2 is:

$$P_{\text{r}} = \frac{P_{\text{t}} \cdot A_{\text{SPAD}} \cdot \chi_{\text{R}}}{2\pi d^2} \tag{3.2}$$

Here, P_{t} is the transmitted optical power, P_{r} is the optical power received by the SPAD, χ_{R} is the reflectivity of the wall, d is the distance to the wall and the area of the SPAD is given by A_{SPAD}.

Wavelength of the laser

The rate at which photons are detected depends on the energy per photon, which in turn is related to the wavelength. As stated in [46], lasers exist at many wavelengths. The most commonly used wavelengths are 850 nm and 940 nm. A 940 nm laser will be used because of a dip in the solar spectrum which will be discussed in section 3.1.2. The energy per photon is:

$$E_{\text{photon}} = \frac{hc}{\lambda} \tag{3.3}$$

Here, c is the speed of light through vacuum, h is the Planck constant and λ is the wavelength of the photons. From this, the photon detection rate due to signal photons is obtained, assuming a small opening angle.

$$R_{\text{photons,sig}} = \frac{P_t \cdot A_{\text{SPAD}} \cdot \chi_{\text{R}}}{2\pi d^2} \frac{P_{\text{pd}}}{E_{\text{photon}}} \tag{3.4}$$

Here, P_{pd} is the photon detection probability.

However, if the opening angle is a significant fraction of a hemisphere, a different formula is needed. The surface becomes an integral, which is evaluated in appendix C. For Lambertian surfaces, which the skin is assumed to be, a cosine is introduced. The integral also results in a cosine, leading to (see also [71, p. 29]):

$$R_{\text{photons,sig}} = \frac{P_t \cdot A_{\text{SPAD}} \cdot \chi_{\text{R}} \cdot \cos^2(\theta)}{2\pi d^2} \frac{P_{\text{pd}}}{E_{\text{photon}}} \tag{3.5}$$

Example

To get a feel for the approximate order of magnitude, the photon rate for an example system is calculated. If a laser is used with peak transmission power $P_t = 2$ mW, a SPAD with a radius of 5.0 µm (which implies an area $A_{\text{SPAD}} = 7.9 \times 10^{-11}$ m^2), an opening angle of 25°, a target distance of 1 m and a photon detection probability of 0.01 at the wavelength of 940 nm, the reflectivity of the material is about 0.4, the photon rate will be approximately 1×10^3 photons per second.

This tells us the total photon rate detected by the SPAD without ambient light. However, ambient light is almost always present. Next, the average ambient light rate is calculated.

3.1.2. Photon rate due to ambient light

Given the target application of use by consumers, a realistic worst-case real-life scenario needs to be chosen. In this subsection, sources of noise are listed that can be encountered in real life. For one selected scenario the photon rate is calculated.

There is no technical upper limit to this rate. A construction involving mirrors, for example can reach arbitrarily high background photon rates.

Sources of ambient light

Noise can come from multiple sources. What are the most intense light conditions that people can be expected to be in? Some typical light sources, with their corresponding intensities, are listed in table 3.1.

Table 3.1: Typical intensities of light in daily life

Full moon on a clear night [72]	0.1 lx
Public areas with dark surroundings (middle of large office by day) [73]	20 lx to 50 lx
Office building hallway/toilet lighting [74]	80 lx
Train station platforms [75]	150 lx
Office lighting [73–75]	320 lx to 500 lx
Overcast day; typical TV studio lighting [73]	1×10^3 lx
Full daylight (without direct sun) [73]	1×10^4 lx to 2.5×10^4 lx
Direct sunlight [73]	3.2×10^4 lx to 1×10^5 lx

As can be seen, even very specific offices (tv studios) do not approach the intensity of the sun. Because of this, from here on sunlight will be used as a source of the highest photon rate.

Direct, diffuse and reflected sunlight
Sunlight can be split into three different categories:

- Direct sunlight, due to a beam from the sun hitting the surface;
- Diffuse sunlight, due to photons redirected by the atmosphere hitting the surface;
- Reflected sunlight, due to surfaces reflecting photons.

These different sources are visualized in fig. 3.3.

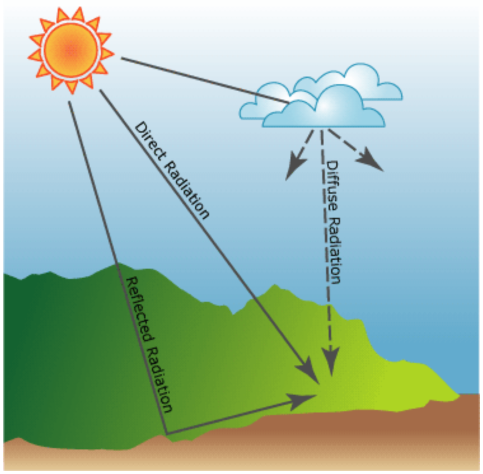

Figure 3.3: Different sunlight processes illuminating surfaces on Earth. Direct radiation is the beam directly from the sun. Diffuse radiation is caused by the atmosphere redirecting photons. Reflection is caused by the surface reflecting photons [76].

Direct sunlight is only relevant if the field of view of the sensor includes the beam from the sun. If it does not, or this beam is blocked by an object, this addition can be ignored.

As said before, reflected sunlight can reach arbitrary intensities depending on the configuration the target device is in. The effect of highly reflective surfaces will be ignored to obtain a number representative of real-world scenarios.

Diffuse sunlight is the only remaining source, but the intensity is related to many factors, such as, but not limited to, air pressure, carbon dioxide concentration, time and place on earth. All of these factors should be taken into account. For this, the American Society of Testing and Materials reference spectra. A proper worst-case scenario is selected in appendix D, for the given bandwidth of 920 nm to 960 nm. Two intensities are obtained:

$$P_{\text{direct,ambient}} = 11.595\,\mathrm{W\,m^{-2}} \mathrel{\widehat{=}} 120\,\mathrm{klx} \tag{3.6}$$
$$P_{\text{diffuse,ambient}} = 0.351\,\mathrm{W\,m^{-2}} \mathrel{\widehat{=}} 3.6\,\mathrm{klx} \tag{3.7}$$
$$\tag{3.8}$$

The power due to diffuse ambient light holds for a point. Given that the light is diffuse, it will arrive equally from every direction. Thus, the field of view should be taken into account as a fraction of a full sphere. Given the opening angle of the SPAD θ_{max}, the arriving sunlight fraction is found as:

$$F_{\text{fov}} = \left(\frac{2\theta_{\text{max}}}{2\pi}\right)^2 \tag{3.9}$$

This leads to the following photon rate:

$$R_{\text{photons,ambient}} = P_{\text{diffuse}} \cdot F_{\text{fov}} \cdot A_{\text{SPAD}} \cdot \frac{P_{\text{pd}}}{E_{\text{photon}}} \tag{3.10}$$

Example
For noise as well as signal, it is important to know what the order of magnitude of the photon rate is. Given the parameters as defined above, an opening angle of about 25°, and photon detection probability, photon wavelength and SPAD area as defined in section 3.1.1, the photon rate due to sunlight

is equal to approximately 1×10^5 photons per second. This is approximately a thousand times more than the laser, which means recovery is not trivial.

These are the average photon arrival rates. Next, the variance of these rates is investigated.

3.2. Photon arrival rate variance

Now that average arrival rates are known, a small piece of the recovery algorithm should be explained to understand why the variance is relevant. As seen from the last two sections, the worst-case scenario shows that the ratio between the laser photon arrival rate and the ambient photon arrival rate is low. If the laser is turned off, a certain amount of photons will arrive at the SPAD. Turning the laser on will only result in a small increase of received photons. Neither of these scenarios contains any information related to the distance of the target. However, there is a time delay in the changing of the average photon rate. The distance to the target is directly related to this time delay. However Figure 3.4 shows two scenarios. The first shows a small increase of a noisy signal, where it is difficult to see the exact position that the laser transitioned. The second shows the same increase with less noise. The transition is more obvious. Intuitively, **the variance of both rates is related to how well one can estimate the exact time of transitioning**, and thus this what the rest of this section is about.

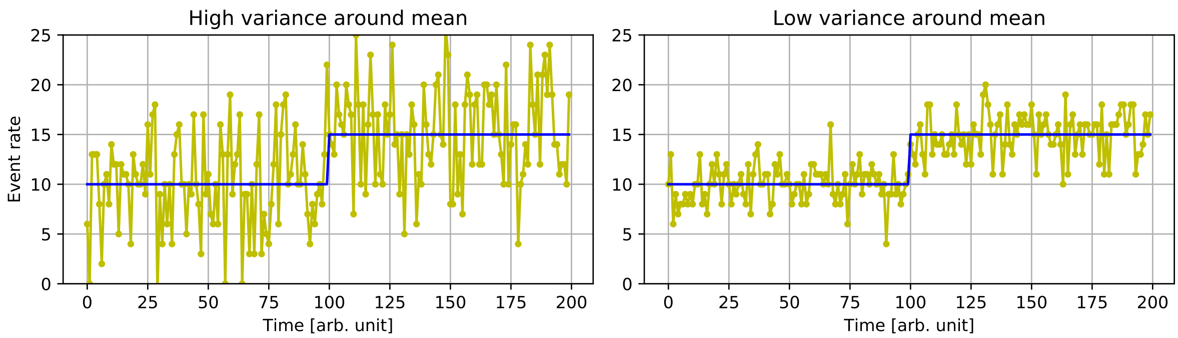

Figure 3.4: Different variances around a changing mean. The moment in time when the average changes is much easier to see in the right graph, where variance is low, than in the left graph, where variance is high.

Why photon arrival times are described by a Poisson process

The amount of photons arriving within an interval is a typical example of a Poisson process [59]. The validity assumptions of the Poisson process all hold:

- Photons arrive independently, i.e. the arrival of one photon does not affect the probability of when the next photon will arrive;
- The average photon arrival rate should be constant during the measurement interval; this implies that either the measurement interval should be short or the environmental conditions should not change too much, otherwise this assumption will no longer hold;
- Two photons cannot arrive at the same instant, they arrive after the other given that the time interval is short enough.

Given that photon arrival times can be described by a Poisson process, and assuming an average arrival rate of R, the variance of the rate is also R, and the standard deviation σ is given by $\sqrt{R}$. In other words, **as the rate increases, the standard deviation of this rate increases with a square root**. This gives some indication that a higher rate gives lower uncertainty.

This holds for any rate. Given that rates are independent, their properties sum nicely as well. Given a photon rate due to ambient light and the laser, the total average photon rate is defined as:

$$\mathrm{E}\left[R_{\mathrm{t}}\right] = \mathrm{E}\left[R_{\mathrm{a}}\right] + \mathrm{E}\left[R_{\mathrm{l}}\right] \tag{3.11}$$

As seen in section 3.1.1 and section 3.1.2, the ambient rate is huge compared to the laser rate. The standard deviation of R_{t} is thus mostly due to the ambient rate and can be simplified accordingly.

$$\mathrm{Var}\left[R_\mathrm{t}\right] = \mathrm{Var}\left[R_\mathrm{a}\right] + \mathrm{Var}\left[R_\mathrm{l}\right] \Rightarrow \sigma_\mathrm{t} = \sqrt{\sigma_\mathrm{a}^2 + \sigma_\mathrm{l}^2} \approx \sigma_\mathrm{a} \tag{3.12}$$

3.2.1. SPAD saturation effects

However, a high rate comes with other effects. As described in section 2.3, a SPAD has some dead time after detecting a photon, during which the SPAD needs to be reset. The assumption is made that SPADs are used with an active quench-rebiasing circuit, which makes the dead time fixed (i.e. non-paralyzing, see section 2.3.5). This means that photons arriving during dead time are ignored. This changes the distribution of detected photon arrival times. For a typical Poisson process, the time between two arrivals is given by the exponential distribution. An example of this distribution, and thus the probability of a certain time interval between two-photon arrivals, is shown in fig. 3.5a. If the SPAD suffers from dead time (for instance 0.5 time units), the probability density would change to the distribution shown in fig. 3.5b [60].

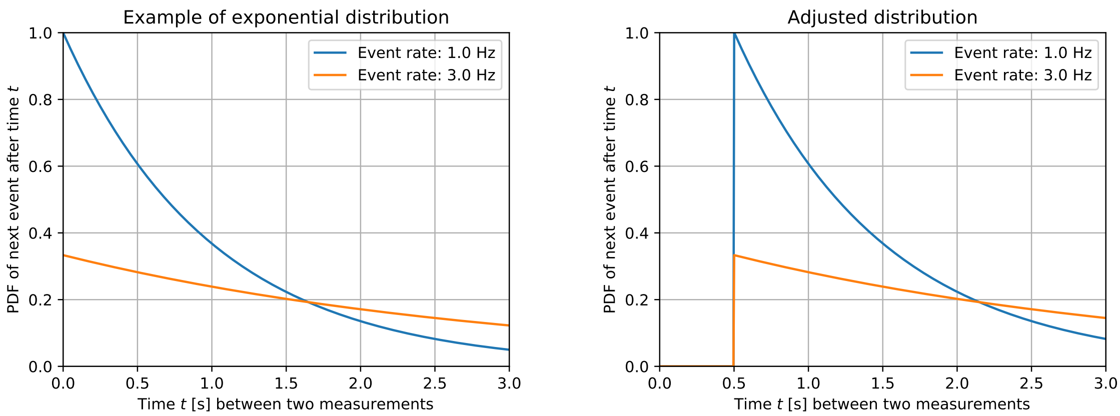

(a) Without dead time

(b) With dead time

Figure 3.5: Exponential distributions and the effect of dead time. The distribution shifts to the right when dead time is introduced.

Here, the part of the PDF before $t = 0.5$ is fixed to zero, and the amplitude is corrected such that the total integral still sums to one. This correction factor is the fraction of ignored photons. Thus, given a photon rate R_o, a new average photon rate R_n is defined in eq. (3.13).

$$R_\mathrm{n} = \frac{R_\mathrm{o}}{1 + \tau_\mathrm{dead} \cdot R_\mathrm{o}} \tag{3.13}$$

This rate reduction implies a change of variance as well. However, this change is not directly given by the Poisson distribution anymore, since the effect of dead time has modified this distribution. The standard deviation of observed counts in a certain time interval $(R_\mathrm{x} \cdot T_\mathrm{obs})$ is given as [60]:

$$\sigma^2(R_\mathrm{new} \cdot T_\mathrm{obs}) = \frac{R_\mathrm{old} \cdot T_\mathrm{obs}}{(1 + R_\mathrm{old}\tau_{NP})^3} + \left(1 + \frac{2}{3}R_\mathrm{old}\tau_{NP} + \frac{1}{6}R_\mathrm{old}^2\tau_{NP}^2\right) \cdot \frac{R_\mathrm{old}^2\tau_{NP}^2}{(1 + R_\mathrm{old}\tau_{NP})^4} \tag{3.14}$$

In short, this means that the relative variance of the rate drops with increasing illumination until the SPAD starts becoming saturated. From this point on the mean value of detected photons will stop increasing. From an intuitive point of view, this makes sense because if 1000 photons hit a surface each second, but the device needs 10 seconds of recovery, then after 10.00 seconds it will take a short amount of time for the next photon to arrive.

For clarity, the effect of decreasing variance is visualized in fig. 3.6b. Figure 3.6a shows the rate becoming constant. A (near-)constant rate means that a small increase (for instance due to the laser) does not show in the output. Since the distance measurement is based around measuring a small difference in rate, this will become even harder. Thus, a trade-off is found; higher rates are desired

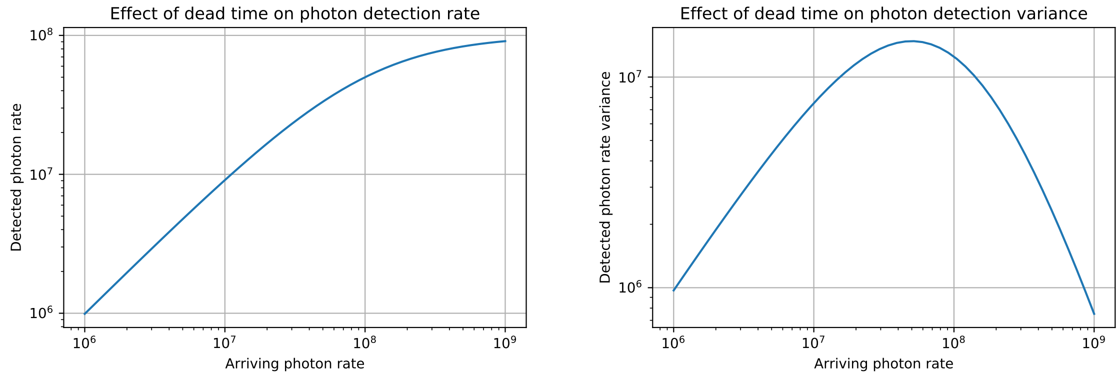

(a) Average photon arrival rate (b) Variance of photon arrival rate

Figure 3.6: Effects of non-paralyzing dead time on SPAD with 10 ns dead time. Due to saturation, the photon rate saturates. The variance of the arrival time drops significantly as the time between two photons becomes easier to predict.

because of the square root in the standard deviation, but lower rates because of saturation and compression of the signal. This problem is solved by setting an upper limit to the photon arrival rate. **The detectable photon arrival rate, when dead time is taken into account, should be at least 95 % of the actual photon arrival rate**.

Now that some effects on SPADs have been discussed, and typical photon rates due to laser and ambient light are known, the algorithm can be discussed that will handle all photons and produce a distance.

3.3. Recovery algorithm

3.3.1. A simple example

As has been discussed before, photon arrival contains no information in and of itself, relating to the distance to the target. Depending on the type of laser, many algorithms can be found that detect the target distance.

The simplest algorithm would involve a sequence of narrow high-power pulses emitted by the laser, each pulse several picoseconds long, and the pulses repeated after several nanoseconds, in high intensity, as shown in fig. 3.7. Here, every pulse is 6 ps long, which translates to 1 mm distance resolution. The SPAD would trigger more often when this narrow pulse arrives back from the target. However, lasers that emit such narrow pulses are difficult to create. Turning the laser off and on as fast as possible is much easier. However, the pulse emitted will then be somewhere between a block pulse and a sine, with some non-symmetrical aspects. The effect of the waveform is elaborated upon in section 3.5, with optical measurements of such a laser shown.

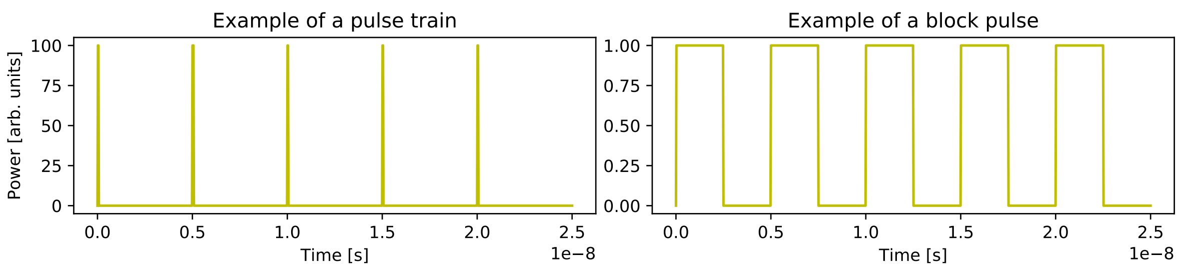

Figure 3.7: Different laser pulses: a pulse train and a block pulse. A pulse train with short pulses is more difficult to reproduce with conventional lasers

Processing the raw SPAD data consists of five steps. These will be explained with a small example. In this example, a SPAD is used with a dead time of 5 ns, and a laser with a switching frequency of 200 MHz pulsing with a sine wave. For clarity of explanation, the signal and noise photon rates are not based on realistic values. In a realistic scenario, one would not be able to distinguish between noise and signal photons. In this example, however, this difference is shown.

The first step involves the SPAD detecting many photons. This is shown in fig. 3.8.

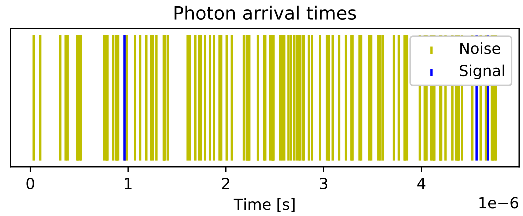

Figure 3.8: Example: 4.8 μs of photon arrivals on a single SPAD

Each photon arrival occurs some time after a laser pulse started. If the assumption is made that the distance to the target is fixed, i.e. the measurement happens in a quasi-static environment, then all laser pulses arrive back with the same phase offset.

The second step is determining the phase offset between each photon and the laser pulse. Furthermore, within one laser pulse, the laser is sometimes on and sometimes off. Thus, the expectation is that during one laser period, some phases (i.e. those corresponding to the laser being on) are more likely to occur than others.

For the example shown in fig. 3.8, the phase is shown in fig. 3.9. The phase is calculated given the arrival time of a photon t_p and the laser period T_L as:

$$\phi = \frac{t_p \mod T_L}{T_L} \cdot 360^\circ \tag{3.15}$$

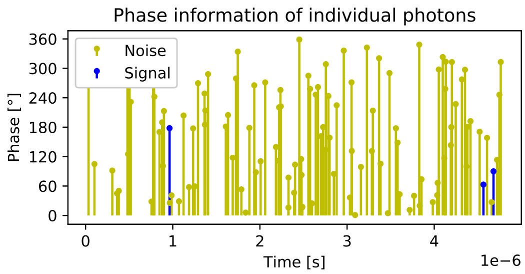

Figure 3.9: Example: phase information for photon arrival times

The third step is collecting the phase information. This is then done through a histogram. The histogram shows the number of photons arriving with a certain phase. In this example, 360 bins are used, so an accuracy of 1 degree can be obtained. The amount of bins is typically given by the time of a laser pulse divided by the resolution of the time-to-digital converter (TDC), and the achievable resolution is therefore limited:

$$B = \frac{T_L}{\tau_{\text{tdc}}} \tag{3.16}$$

A way of increasing the resolution is given in section 3.6. An example of a histogram is shown in fig. 3.10.

This histogram is not particularly useful since it contains only three photons that originate from the laser. A more useful example is shown in fig. 3.11.

In the fourth step a correlation is performed to determine the phase shift. The dot product of the measurement and a cyclically shifted sine wave is calculated. A correlation of a sine with a noisy sine will result in a sine. Noise is transformed into phase and amplitude noise of the correlated signal.

The fifth and last step is to calculate the phase offset of the maximum correlation. This index corresponds to the target distance. A translation step is necessary to yield the actual distance:

$$d_{\text{target}} = i \cdot \tau_{\text{tdc}} \cdot \frac{c}{2} \tag{3.17}$$

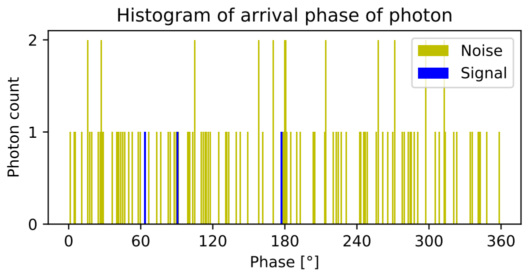

Figure 3.10: Example: histogram created from phase information example

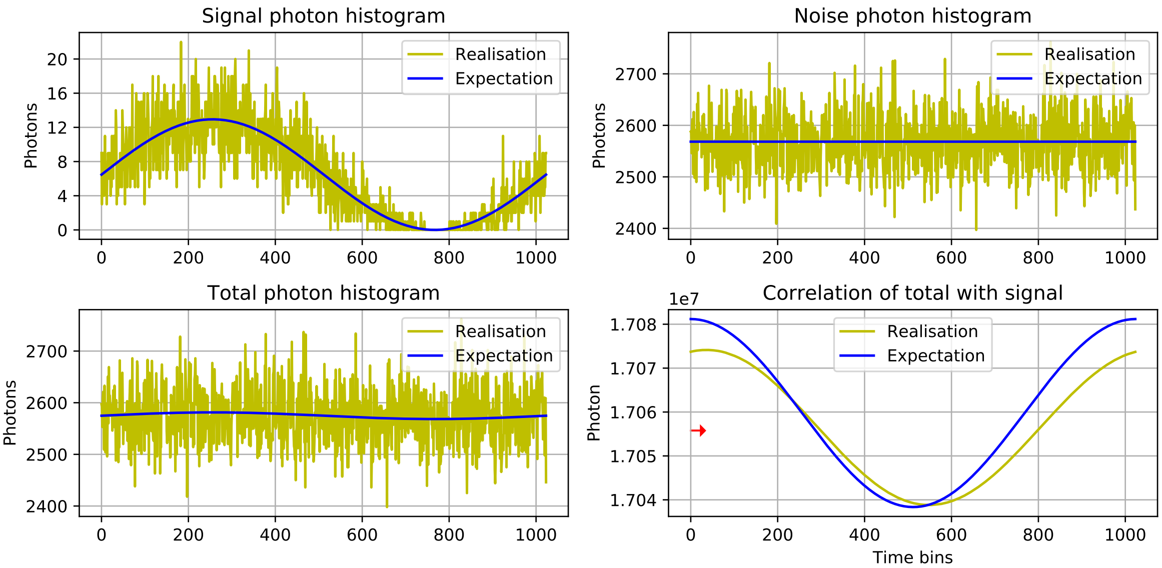

Figure 3.11: Example: signal and noise photon histograms for sine pulse

The remainder of this section analyzes this algorithm to understand how well it will perform under different signal to noise conditions.

3.3.2. Algorithm analysis

In order to derive the expected error of detection (for a sine wave), the expected height of histogram bins due to signal and noise first needs to be understood. Then, a standard deviation can be calculated.

As specified before, the laser is assumed to emit a sine wave, which in section 3.5 is shown to be a good approximation of most lasers.

Both signal (laser) and noise (ambient) photon arrival times are Poisson processes. A Poisson process with high λ approximates a normal distribution.

$$\text{Poiss}\left(\lambda\right) \approx \mathcal{N}\left(\mu = \lambda, \sigma^2 = \lambda\right) \tag{3.18}$$

Thus, the signal and noise rate can be approximated by two normally distributed variables:

$$\text{Poiss}\left(R_\text{s}\right) \approx \mathcal{N}\left(\mu = R_\text{s}, \sigma^2 = R_\text{s}\right) \tag{3.19}$$
$$\text{Poiss}\left(R_\text{n}\right) \approx \mathcal{N}\left(\mu = R_\text{n}, \sigma^2 = R_\text{n}\right) \tag{3.20}$$
$$\text{Poiss}\left(R_\text{t}\right) \approx \mathcal{N}\left(\mu = R_\text{s} + R_\text{n}, \sigma^2 = R_\text{s} + R_\text{n}\right) \tag{3.21}$$

Given photon arrival rates R_x and the amount of bins B:

$$B = \frac{T_\text{L}}{\tau_\text{tdc}} \tag{3.22}$$

The corresponding expected amount of photons in a bin Q_{x} is given by:

$$Q_{\text{x}} = \frac{R_{\text{x}} \cdot T_{\text{obs}}}{B} \tag{3.23}$$

Given the quasi-static scenario, the photon rate due to ambient light does not change between the start and end of every measurement. This also means that the average value of the photon arrival rate due to ambient light is constant. In this sense, a higher average noise rate does not influence the quality of the measurement. However, with a higher average rate follows a higher standard deviation, from the Poisson distribution, and this does influence the measurement. As such, to determine the standard measurement error, the ambient photon rate average can be ignored. Furthermore, the standard deviation of the signal is tiny compared to the noise, which means the variation of the signal rate can be ignored as well.

Given measurement time T_{obs} and that these photons are distributed over B bins, the value in one bin of the histogram can be described by:

$$Q = \mathcal{N}\left(\mu = \frac{R_{\text{s}} \cdot T_{\text{obs}}}{B}, \sigma^2 = \frac{R_{\text{n}} \cdot T_{\text{obs}}}{B}\right) \tag{3.24}$$

Here, R_{s} depends on the phase offset and bin index. The question arises how this bin height distribution is related to the standard measurement error, which is the error in the maximum of the correlation.

By using the derivative of the correlation with respect to the index, the standard deviation of the error around the actual distance can be expressed in terms of the number of detected photons due to signal, the amount of detected photons due to noise and the period of the laser [77]:

$$\sigma^2\left(\Delta i \cdot \tau_{\text{tdc}}\right) = \frac{B}{(2\pi)^2} \frac{\tau_{\text{tdc}}^2}{\text{SNR}} \tag{3.25}$$

In other words, next to the number of photons arriving, only the oscillation frequency of the laser is related to the performance of the algorithm. If the SNR is filled in, this formula becomes a bit larger:

$$\sigma^2\left(\Delta i \cdot \tau_{\text{tdc}} \cdot \frac{c}{2}\right) = \frac{Q^2}{(2\pi)^2} \frac{R_{\text{n}}}{R_{\text{s}}^2} \frac{\tau_{\text{tdc}}^2}{T_{\text{obs}}} \tag{3.26}$$

In this formula, the standard deviation of detection in meters is expressed. If the formulas for the rates calculated in section 3.1 are included, the formula becomes more complicated:

$$\sigma_{\text{m}} = \frac{c}{2}\sqrt{\frac{hc}{\lambda}} \frac{T_{\text{laser}} \cdot d^2}{\sqrt{T_{\text{obs}} N_{\text{SPAD}} \pi r_{\text{spad}}^2 P_{pd}}} \frac{\theta}{\cos^2(\theta)\, \chi_{\text{R}}} \frac{\sqrt{I_{\text{a}}}}{P_{\text{t}}} \tag{3.27}$$

Here, I_{a} is the intensity of the ambient light, N_{SPAD} the amount of SPADs in naive configuration (discussed later) and P_{pd} the probability of photon detection by the SPAD. The standard deviation of the measurement depends linearly on the oscillation frequency of the laser, squared on the target distance and linearly on the power of the laser. Also, the number of SPADs and the observation time are in a square root. This means that results will not get better as fast as the time increases.

The presented formula assumes that multiple SPADs are combined by making no distinction between where a photon hits. Are there ways of combining multiple SPADs in a way that is more powerful than a single SPAD?

3.4. Using multiple SPADS

Until now, all analysis was done using a single SPAD. Intuitively, if more SPADs are used, a better result should be obtained. However, SPADs can be combined in multiple ways. Which one is best?

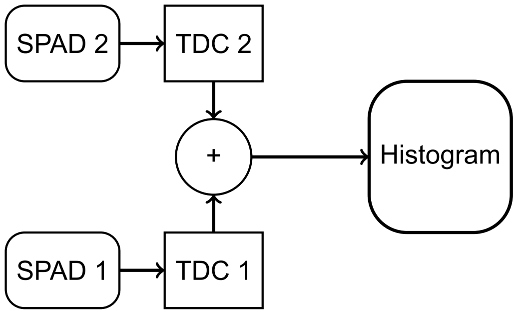

Figure 3.12: Simple combination of TDCs and SPADs: add both pulses to the histogram

3.4.1. Combining histograms

The simplest solution is viewing the SPADs as different devices and if a photon from either SPAD is obtained, fill a single histogram. Effectively, this creates a larger SPAD that does not suffer from dead time. Here, the signal-photon to ambient-photon ratio stays the same, but both rates increase. Because the standard deviation of the noise rises with the square root of the magnitude of the noise, the standard error will increase with the square root of the number of SPADs as compared to a single SPAD. Twice as many SPADs in this solution has the same effect as sampling twice as long.

3.4.2. Triggering on k SPADs

Instead of only increasing the rate of photons, we can also try to increase the SNR. This is shown in fig. 3.13.

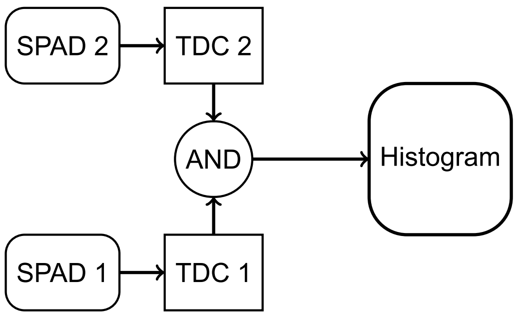

Figure 3.13: 2-trigger system setup: events only happen if both SPADs are triggered within the same bin

One way of doing this is by viewing the arrival of k photons within the same time bin as distinct from only 1 photon.

First look at the case of two photons arriving within the same time interval, on two SPADs. Then, there are four possibilities as to the origins of these two photons, listed in order of probability:

- Both originate from ambient light;
- One originate from ambient light, and the other from the laser;
- Both originate from the laser.

If these events are reduced to a single event which is either noise or signal, the first case would a noise event, but the other two are signal events. The signal and noise events are assumed uncorrelated. Furthermore, because the probability of a hit in 1 bin is very low, the combined probability of the signal and noise events can be added, as the intersection is close to zero. Given the probability of an ambient photon arriving in a time bin P_N, and the probability of a laser photon arriving in a time bin P_S:

$$P_S \ll P_N \tag{3.28}$$

$$P_N \ll 1 \tag{3.29}$$

$$P_T = P_S + P_N - P_S \cdot P_N \tag{3.30}$$

As both P_S and P_N are very small, the last term is approximately zero:

$$P_T \approx P_S + P_N \tag{3.31}$$

Then for two SPADs, the following holds:

$$P_T^2 = (P_N + P_S)(P_N + P_S) \tag{3.32}$$
$$P_T^2 = P_N^2 + 2P_N P_S + P_S^2 \tag{3.33}$$
$$P_T^2 \approx P_N^2 + 2P_N P_S \tag{3.34}$$

If we call an event involving N photons in the same time bin on N different SPADs an N-photon event, then for all N-photon events, following eq. (3.34), the probability of the event originating from the laser is (at least) N times as large as the probability of a single-photon event originating from the laser. However, a two-photon event is much less likely to occur than a one-photon event. Following from section 3.2.1 and given the 95 % requirement:

$$0.95 = \frac{1}{1 + R\tau} \tag{3.35}$$
$$R\tau = \frac{1}{1 + 0.95} \tag{3.36}$$
$$R \approx \frac{0.0526}{\tau} \tag{3.37}$$

And given that the dead time is much higher than the resolution of the TDC, the probability of a hit occurring in one bin is very low. The probability of a k-of-N system being hit by (at least) k photons in the same bin is much lower for small N. Only when N, the number of SPADs used, becomes large is the probability of k-photon events not very low. This is shown in fig. 3.14. In the beginning, more SPADs lead to (almost) linearly more photons. This is why jumps of a factor of 2 can be seen at $k = 1$. However, as the number of SPADs grows, more and more bins are already filled with (more than one) photons. This is observed at more than 1×10^4 SPADs, when the number of photons arriving per second is near the number of bins per second. Then, the only thing that can happen is that more photons arrive in the same bin, which means the graph will shift more to the right.

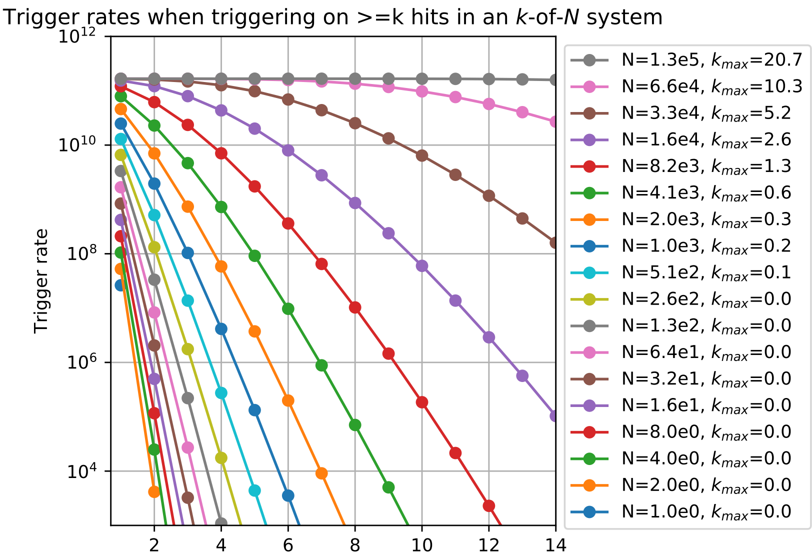

Figure 3.14: Rate of photon arrival in k-of-N system

We can also see that triggering on many SPADs is only useful when many SPADs are used. Since the SNR depends linearly on k, k should be as high as possible. However, a low photon rate means a relatively high standard deviation. This tradeoff is shown in fig. 3.15. On the y-axis, a compound metric is shown consisting of the SNR gain (k) multiplied by the square root of the signal rate.

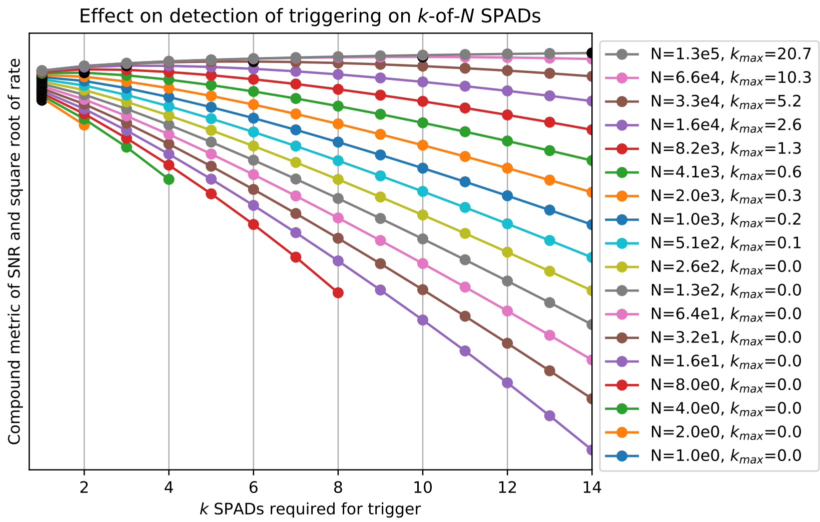

Figure 3.15: SNR versus rate tradeoff

From this graph, we can see that the optimal value of this compound metric is usually $k = 1$, until many SPADs are used. $N = 4096$ is the first point at which a higher k is useful. For a clearer list of Ns and ks, see table 3.2.

Table 3.2: Compound k optimum

N	1	2	4	8	1024	2048	4096	8192	16384	32768	65536	131072
k	1	1	1	1	1	1	2	2	3	6	10	14

The largest gains are had in situations with many SPADs. However, this is given the assumption that $P_T \ll 1$, as stated in section 3.4.2. This is no longer the case for so many SPADs.

3.4.3. Maximal Ratio Combining

The theory of maximal ratio combining [78] states that when combining signals with different signal to noise ratios and different rates, they should be weighed according to their signal to noise ratio. For instance, a signal A with an SNR that is twice as high as another signal B should be twice as important.

Applying this to the given problem: given an event of one photon hitting one SPAD, and another event of N photons hitting N SPADs within one time bin, the latter event should weigh N times as much. In other words, if all photons are counted individually, the theory of maximal ratio combination has already been applied.

3.5. Different laser waveforms

As stated at the start of section 3.3, in the calculations above, the laser was assumed to emit a perfect sine wave. In practice, this will never be the case. The actual waveform of a laser depends on many factors. The waveform emitted by one laser, included with an ST VL6180X [21] at room temperature is shown in fig. 3.16.

As can be seen in fig. 3.17, the correlation changes fundamentally when a block pulse is sent out. Instead of the noise being contained in the phase and amplitude difference of the resulting block pulse, which was the case with the sine wave, the shape of the pulse itself is distorted. This is because a correlation of a block pulse is a summation of half the wave. An index shift in this correlation means one value more on one side, less on the other side will be included in the sum. Because the height of the bin behaves according to a normal distribution, the correlation of this signal is the sum of N random variables: a Wiener process.

Since the point of interest is the top of the block pulse, but the expected correlated wave has no derivative, the standard deviation of the maximum of the correlation cannot be determined.

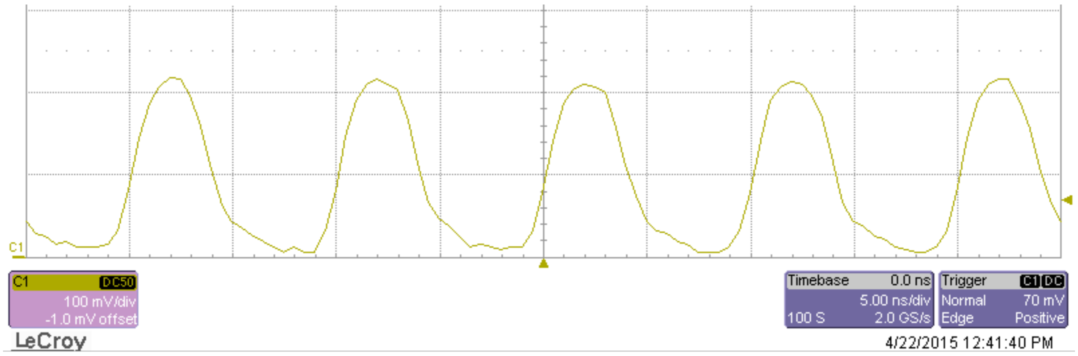

Figure 3.16: Laser waveform of ST VL6180X [79].

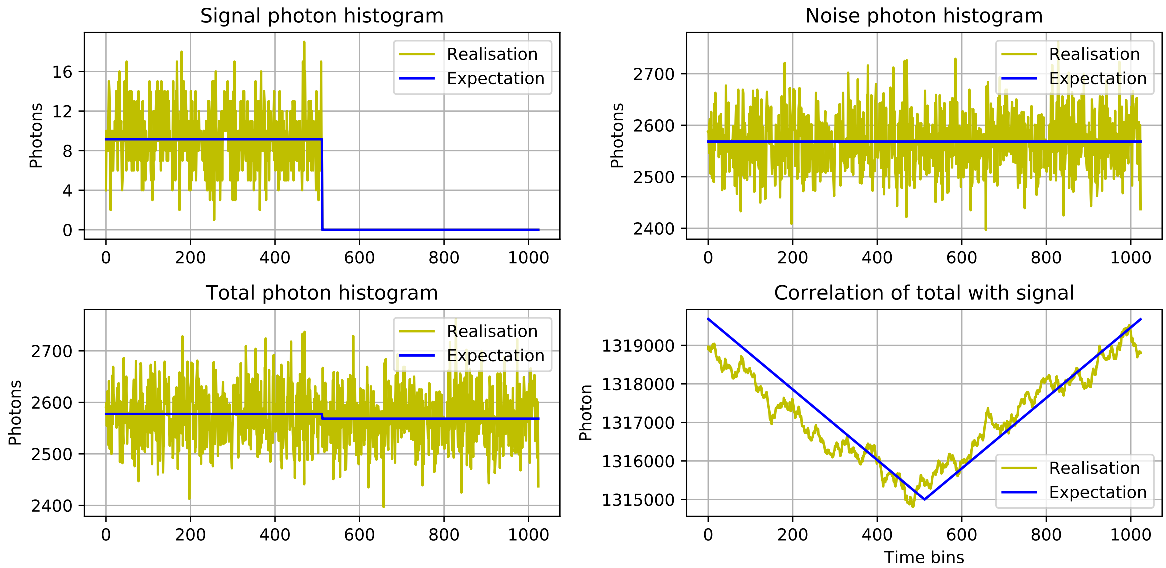

Figure 3.17: Algorithm applied to a block pulse. Instead of a sine, the correlated waveform now is a sawtooth. The maximum of the sawtooth is related to the distance of the target.

An answer relating to the SNR dependence of the standard deviation for block pulses is given by radar technology. As shown in [80], the block pulse is the only waveform where the standard deviation is linearly related to the signal to noise ratio, instead of the square root dependence which holds for any sine-like waveform. This is confirmed by simulations shown in fig. 3.18. Waves in between a block pulse and a sine, like a raised-cosine, behave similar to a sine, only a constant factor better. This is elaborated upon in fig. 4.11.

Thus, the closer to a block pulse the laser can get, the better the measurement results will be.

If the laser emits a sine wave, then the correlation pulse should also be a sine wave. The effect of the shape of the laser pulse is low, as long as a sine wave is used for correlation. Using a block pulse for correlation when a sine is emitted by the laser yields poorer results.

3.6. Lower TDC resolution

A recovery algorithm has been presented that uses a time-to-digital converter of very high resolution. If a resolution of 1 mm is desired, a TDC is required with a resolution of 6 ps. As discussed in section 2.4, these devices are expensive in terms of power and chip area required, as well as being limited in dynamic range and slow (the result of a conversion with a range of several nanoseconds may take tens of nanoseconds to compute).

Because of this, it is desirable to use a TDC with lower resolution. However, a poorer TDC leads to less possible values that can be measured and a larger distance between those values. The dis-

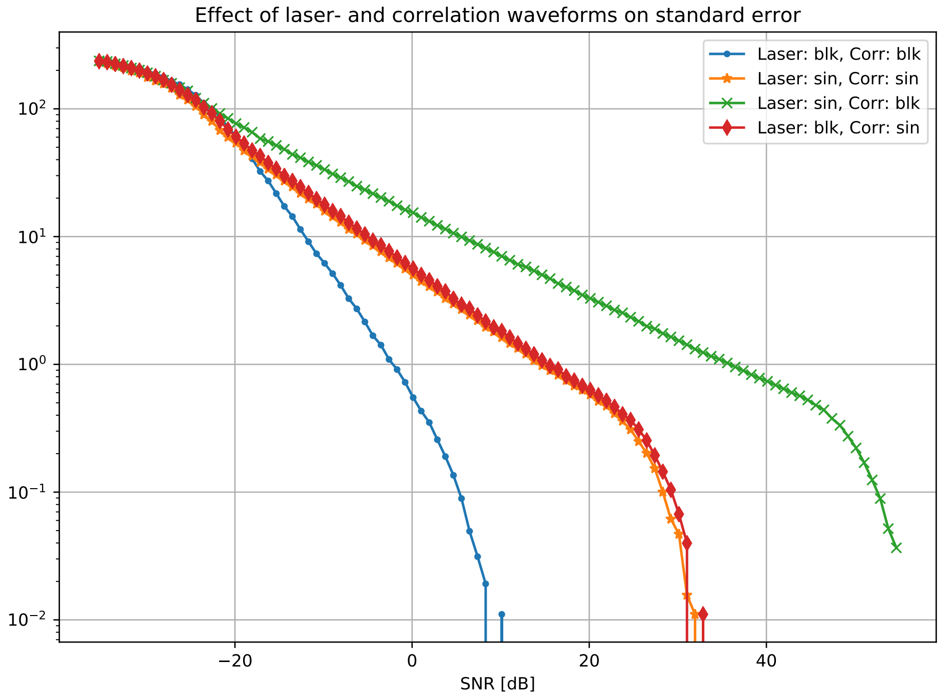

Figure 3.18: Effect of different transmission and detection waveforms on detection. If both the laser and correlation waveforms are square waves, the detection follows a different slope. If the laser sends out a block pulse, then correlation with any wave is just as good or better than if the laser sends out a sine. If the laser sends out a sine wave but the correlation is a square wave instead, detection is much worse.

cretization of the actual measurement result into bins produces quantization noise. Figure 3.19 shows why this is a problem.

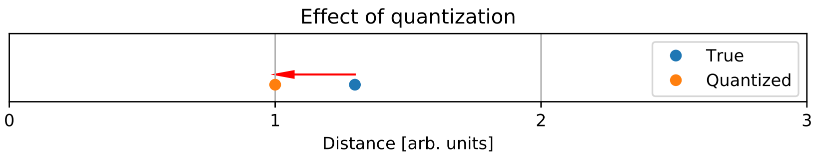

Figure 3.19: Quantization noise visualised. The actual value cannot be represented by the measurement device, and the closest value is chosen.

The formula for standard deviation as stated before does not take this into account. In this section, a new formula for standard deviation is found that does take quantization noise into account. Furthermore, because the standard deviation of the analog measurement does not depend on the resolution of the TDC, system behavior is analyzed when a TDC with lower resolution is used.

3.6.1. Quantization noise

The measurement error may be due to two phenomena

- Quantization with standard deviation σ_q
- Ambient noise with standard deviation σ_n

As standard deviations may not be added, but variances may, the standard deviation of the measurement is

$$\sigma_\text{t} = \sqrt{\sigma_\text{q}^2 + \sigma_\text{n}^2} \tag{3.38}$$

Previous sections worked towards an expression for σ_n, this section will explain the quantization noise σ_q.

The quantization noise can be modeled by a uniform random variable if the variation in signal is large enough. Then, the assumption that noise is not correlated with the signal holds. The average value of this random variable is, of course, equal to zero, as the noise fluctuates between -0.5LSB and 0.5LSB. The standard deviation of a uniform distribution is equal to $\frac{1}{\sqrt{12}}$LSB [59]. Thus, the total standard deviation of a measurement as follows from eq. (3.38) does depend on the resolution, as expected. The standard deviation in meters is as follows:

$$\sigma_{\text{t,m}} = \sqrt{\sigma_{\text{n,m}}^2 + \left(\frac{c}{2}\frac{\tau_{\text{tdc}}}{\sqrt{12}}\right)^2} \tag{3.39}$$

Now, given a much poorer TDC, can the original resolution still be obtained?

3.6.2. Using multiple subintervals per measurement

Now that the effects of quantization noise are known, a technique can be analyzed to achieve the same resolution in a system with a lower measurement resolution. This can be done by averaging. Instead of performing one measurement for the duration of T_{obs}, the algorithm is run multiple time for shorter subintervals. This is shown in fig. 3.20. The result of the measurement is then equal to the average

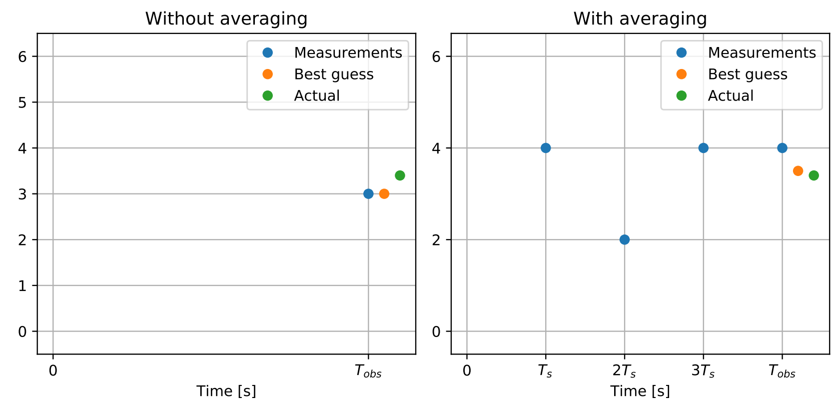

Figure 3.20: How resolution can be improved with averaging. Because of the discretization error, the result of one measurement cannot be better than what is shown on the left. However, even with worse resolution, the error can be smaller if multiple measurements are performed.

of the results of the individual subintervals. For instance, every subinterval would run for $\frac{T_{\text{obs}}}{M}$, and the result of M samples would be averaged to obtain a result with higher resolution.

However, there are limitations regarding the amount of subintervals per measurement, as well as the factor by which the resolution of the TDC can be made worse while still obtaining the same measurement resolution and accuracy, which will be discussed in the rest of this section.

If the resolution of the TDC is equal to its range, which would imply a B of 1, no information can be recovered because all information is thrown away. Two bins are not enough either since sub-resolution averaging cannot be applied: is the true result between the first and second bin, or at the edge (or beginning) of the dynamic range, i.e. in the wraparound? Three bins should be enough, but since powers of two are generally easier, an example using $B = 4$ will be shown.

If the resolution of the TDC is L times worse than in the original system and the measurement interval is split into M subintervals, the standard deviation changes. Per subinterval, the sigma due to ambient noise becomes $\sqrt{M}$ times worse, because the time for the sample becomes M times smaller. However, there are now M subintervals to average, which makes the total σ go down by a factor of $\sqrt{M}$ again. Simplification leads to eq. (3.40).

$$\sigma_{\text{t,m}} = \sqrt{\sigma_{\text{n,m}}^2 + \frac{c^2 \cdot L^2 \cdot \tau_{\text{tdc}}^2}{48 \cdot M}} \tag{3.40}$$

However, when applying this, two initial assumptions are encountered.

The quantization noise should be large enough

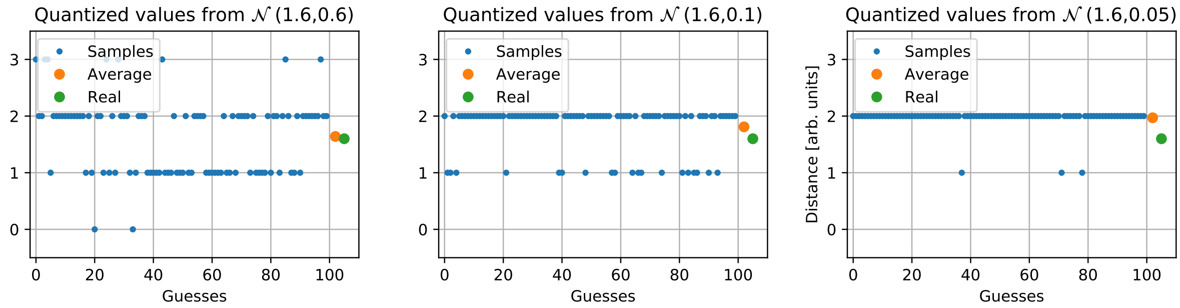

Figure 3.21: Too small quantization noise causes only one value to be output across all measurements.

The assumption was made in section 3.6.1 that the signal is much larger than 1 LSB. If this is not the case (most notably if the TDC has a dynamic range of 2 or 3 bits), then the quantization noise cannot be assumed to be a uniformly distributed random variable. Specifically, if the noise due to ambient light is much smaller than the noise due to quantization, the closest bin will always be the result of the subinterval. Averaging is then useless because (nearly) all subintervals have the same index. This is shown in fig. 3.21. Note that this is only relevant if the resolution of the TDC is very low and the noise on the bin height is relatively small.

This problem can be solved by introducing artificial noise with a magnitude of 1 LSB. Then the noise will be larger than 1 bit in the quantizer, and averaging will work. One way of implementing this noise is by randomly delaying the start of the laser pulse with up to 1 LSB of the TDC.

The ambient noise per subinterval should not be too large

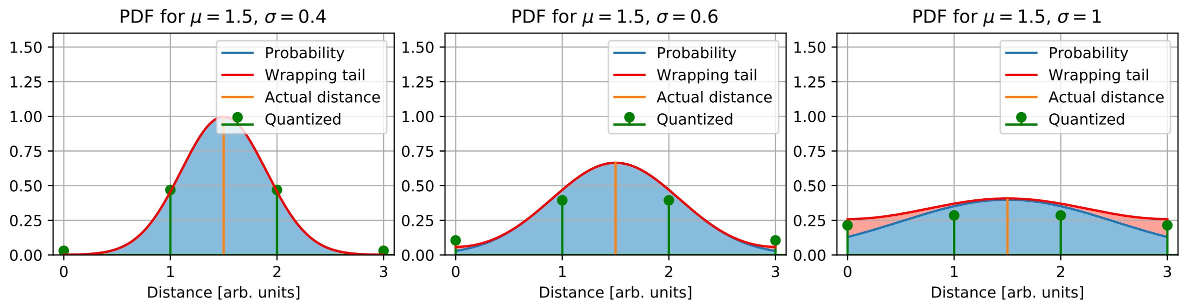

Figure 3.22: Quantized probability density function with different σ. The tail wraps around causing a near-uniform distribution of measurement results. Recovering the actual distance from results distributed like this is impossible.

On the other hand, too much noise intuitively yields poorer results as well. With a high M comes a low time per subinterval. While the accuracy of one sample is small, averaging many samples results in a high accuracy measurement. However, if the time per subinterval is too small, and the probability distribution approximates a uniform distribution, recovery is no longer possible. While no exact lower bound was found, recovery is certainly possible if $6\sigma_{\text{subinterval}} > \frac{1}{2}T_{\text{laser}}$, because events outside the (arbitrary) 6σ are unlikely. This is shown in fig. 3.22, where the first figure shows that nearly all of the found values will be 1 and 2. The second figure shows the unlikely results, 0 and 3, have non-negligible height. The third figure, however, shows an additional problem. The tail end of the distribution wraps around. If this tail end is significant, the distribution will quickly approach a uniform distribution. If all four bins are nearly equally likely, recovery is impossible.

As such, given a low-resolution TDC, the optimal action to take depends on the signal to ambient ratio. If the SNR is high, a high-resolution measurement can be obtained by averaging a lot of subintervals (high M). However, given a low SNR, the condition in section 3.6.2 may not be satisfied for a high M. In this case, a better result can be obtained by using a lower M, however, the result will be worse than with a high SNR.

This can be detected as the subintervals are coming in by looking at the distribution of individual sample results. If they are too uniformly distributed, some histograms may be combined for better optimal results.

4

Simulation results

To confirm the theoretic results presented in the previous chapter, a simulation proves useful. To this end, the system was simulated in three ways. Firstly, all photon bins were simulated individually. This means that for every SPAD, for every bin of the TDC, the amount of photons hitting during that interval is calculated.

However, with a low SNR and a relatively high measurement time, the amount of bins that need to be simulated is very high. Using the exponential distribution relating to the arrival time of photons, the need to simulate every bin is translated into a need to simulate every photon.

Again, simulating an environment with a lot of light, hundreds of millions of photons, is very slow. To this end, the simulation was simplified again, this time the histogram is directly simulated. This is much cheaper. Many simulations can be run, leading to an accurate estimate for the standard deviation of the measurement.

This chapter describes the setup of these simulations in some detail, focussing on the last (and best) simulation tool.

4.1. Simulating very small time intervals using the Poisson distribution

The first simulator is the easiest. fig. 4.1 shows the block diagram of this simulator. This simulator is covered by a set of inputs, a way of processing these inputs, and produces an output.

4.1.1. Inputs

The simplest simulator takes the following parameters as input:

- Laser photon arrival rate R_l;
- Ambient photon arrival rate R_a;
- Resolution of the TDC τ_{tdc};
- Laser flashing period T_L;
- Simulated target distance d;
- Measurement time T_{obs};
- Amount of SPADs simulated N_{SPAD};
- Amount of SPADs on which to trigger, which in this simulator is always fixed to 1.

4.1.2. Procedure

Given these inputs the amount of bins to simulate is calculated as:

$$B = \frac{T_{\text{obs}}}{\tau_{\text{tdc}}} \cdot N_{\text{SPAD}} \tag{4.1}$$

With a high resolution in the order of picoseconds, and a measurement time in the order of tens of milliseconds or longer, this may grow large. Two Poisson distributions are created, one as $N_{\text{RNG}} =$

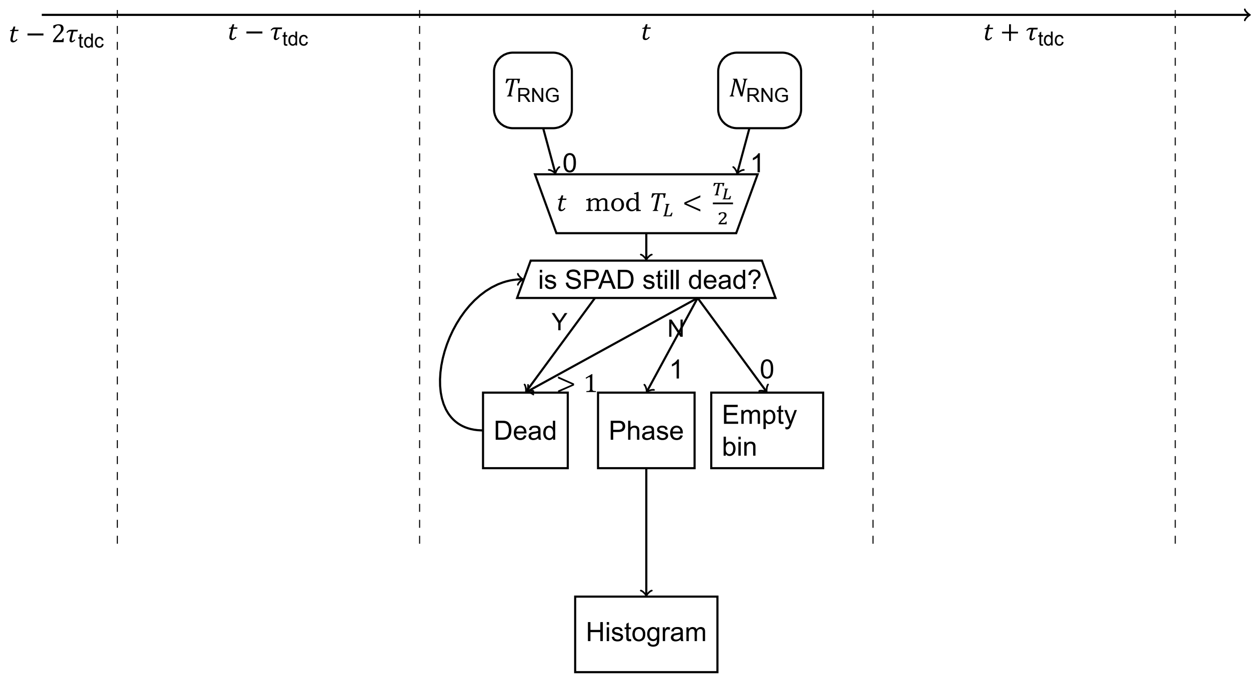

Figure 4.1: Block diagram of Poisson simulator

Poiss $(\lambda = R_N \cdot \tau_{\text{tdc}})$ and one as $T_{\text{RNG}} =$ Poiss $(\lambda = (R_S + R_N) \cdot \tau_{\text{tdc}})$. One or the other is selected depending on whether the laser light is visible in this time bin. The laser is assumed to be on for half the time, and off for the other half of the time; in other words, it is assumed to generate a block pulse and not a sine-like wave. If the laser is on, a random number from the R_N-based Poisson distribution is drawn.

The drawn number is highly likely to be zero, as the dead time of the SPAD is huge compared to the time width of one bin; to avoid saturation, the average time between two photons should be at least one order of magnitude larger than the dead time. However, if the drawn number is not zero, then one of three events has occurred:

- One or more photons arrive while a photon has also arrived within t_{dead}, which means the SPAD cannot detect these photons; all arriving photons are ignored;
- The SPAD has not been hit by a photon within t_{dead} so the arriving photon is counted;
- If more than one photon has arrived within one bin while the SPAD is alive, then one counts while the rest is ignored, as the SPAD cannot distinguish between one or two photons arriving shortly after each other. This is very unlikely given the average time between photons is orders of magnitude larger than the duration of 1 bin.

The photons that are detected are collected in a histogram. This histogram is post-processed by the algorithm described in section 3.3. Since the assumption was made that the laser pulses with a perfect block pulse, the correlation of the histogram is reduced to a simple summation of half of the histogram. N correlations are calculated, and the maximum is found. This maximum is compared to the actual phase of the target that was used to generate the laser's block pulse, and compared as follows.

For a found maximum m and an actual phase p, the measurement error e is given by the following formula:

$$e = |m - p| \tag{4.2}$$

Because the expected error has a mean of zero, m may be larger (1) or smaller (2) than p. However, this does not take wrapping into account. If the actual phase is positive, but small, then the found maximum may be very large, as shown in fig. 4.2c.

This is why the minimum of two errors needs to be chosen: one with wrapping and an error without wrapping. A better formula is thus:

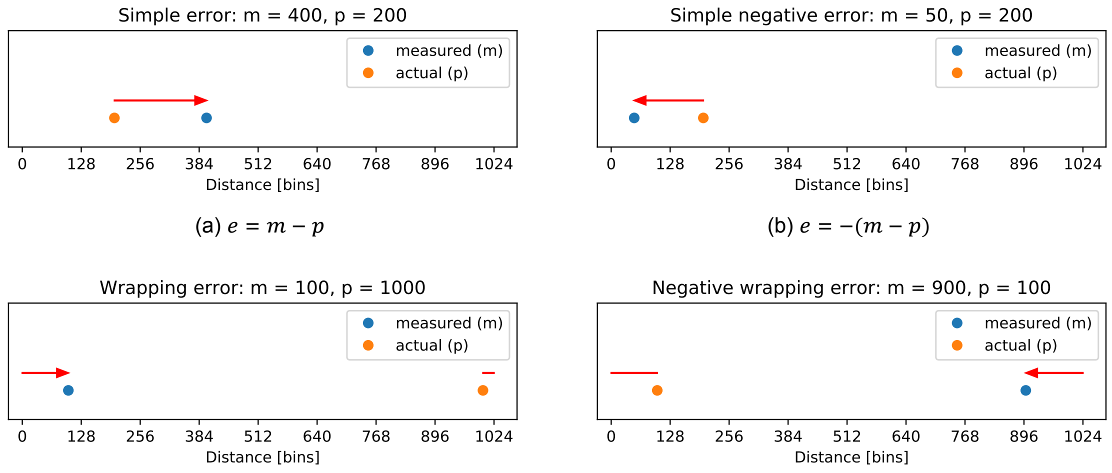

(a) $e = m - p$

(b) $e = -(m - p)$

(c) $e = 1024 + (m - p)$

(d) $e = 1024 - (m - p)$

Figure 4.2: All possible types of measurement errors that can occur

$$e = \min\left(|m - p|, N - |m - p|\right) \tag{4.3}$$

The error of the measurement can thus be at most $\frac{N}{2}$, since if $|m - p| > \frac{N}{2}$ then $e = N - |m - p| < \frac{N}{2}$ must be smaller.

If there is no signal and the error is uniformly distributed between the minimum error (0) and the maximum error($\frac{N}{2}$), the worst-case average error is $\frac{N}{4}$.

4.1.3. Number of measurements per datapoint

For estimation of the standard error, the following formula can be used, given M measurements:

$$\sigma_{\text{meas}} \approx \sqrt{\frac{1}{M}\sum_{i=0}^{M} e_i^2} \tag{4.4}$$

where e_i is the error in measurement i. Intuitively, a higher M gives a better estimate of the standard error. However, the already high simulation time is multiplied by M for every simulation. As this simulation is computationally expensive, only low values of M are used.

4.1.4. Time and memory complexity

Each measurement contains (at least) 1 SPAD, a varying T_{obs}, and a photon arrival rate of around 1×10^7 photons per second. For every time bin, one (or two) random numbers need to be drawn. Thus, the compute complexity is extremely high if measurement times in the order of tens of milliseconds need to be simulated.

The memory complexity is low, as all sampled photons are added to a small fixed-size histogram. Only if extremely low laser frequencies are used will the histogram contain many bins and use more data, but this is typically not useful.

The time complexity is very high, as for every SPAD for every simulated second, the amount of random numbers drawn is equal to $\frac{1}{\tau_{\text{tdc}}}$. For a resolution of 1 mm, this gives over 1×10^{12} random numbers per SPAD per simulated second. The correlation performed afterwards consists of B^2 multiplications (of in total, $2B$ elements), B additions and finding the maximum of B elements. Here, B is the number of bins, or the period of the laser pulse divided by the resolution of the TDC. As the amount of random numbers that can be simulated per second is in the order of 1×10^7, there are 1×10^{12} bins per second, and the simulation time should be in the order of hours at most, simulating more than a

Table 4.1: Parameters for simulated system

Laser pulse frequency	2×10^8 Hz
Dead time	2×10^{-9} s
Number of SPADs	128
R_s	$1.45 \times 10^7\ \mathrm{s}^{-1}$
R_n	$1.18 \times 10^7\ \mathrm{s}^{-1}$
T_{obs}	1×10^{-7} s to 1×10^{-4} s

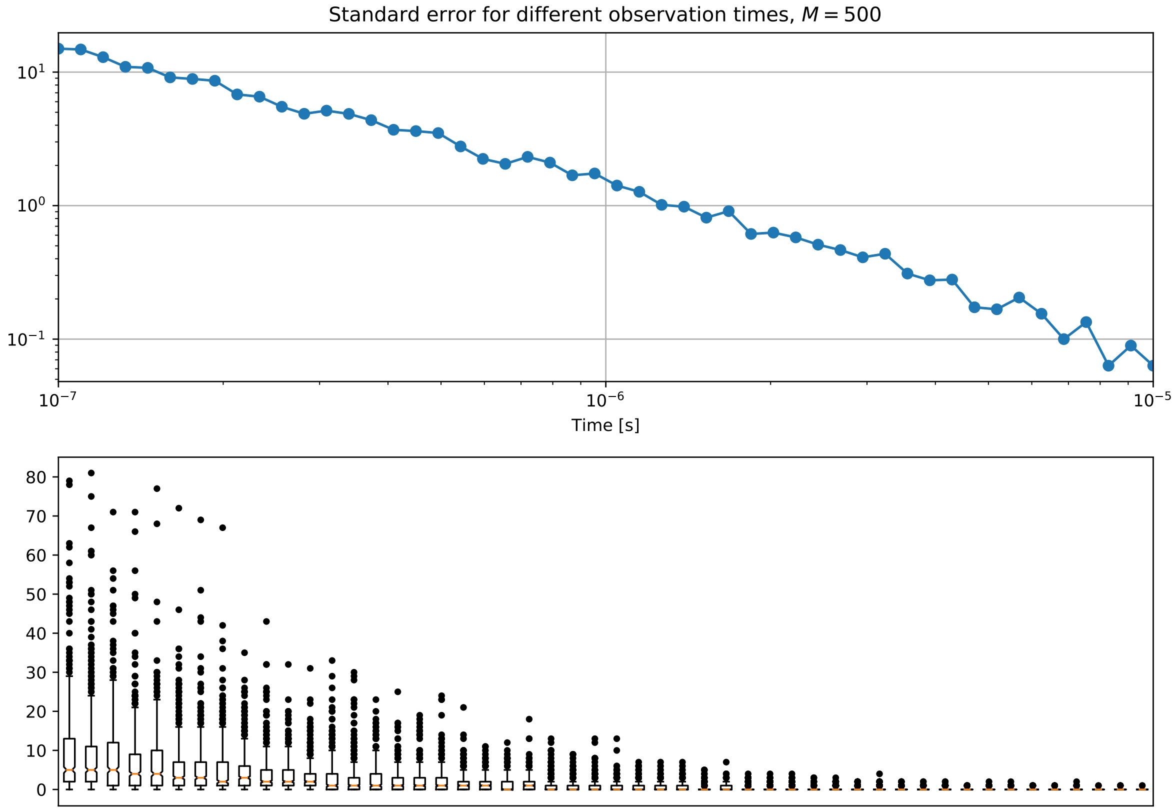

Figure 4.3: Results of poisson simulated system

few microseconds is impossible in this configuration. For a high enough SNR, this can still produce sensible data.

Figure 4.3 show some results for the system described in table 4.1. The upper graph shows the standard deviation, calculated as $\sigma \approx \sqrt{\frac{1}{500}\sum_{i=0}^{500} e_i}$, for 100 different times. All other parameters are kept equal. The lower graph shows boxplots of the individual errors. The box shows the first to third quantile of the errors, the whiskers show the 10 % to 90 % values. The notch shows the median. Numbers outside the 10 % to 90 % range are shown as single dots.

While these graphs lack the accuracy to draw exact conclusions, a trend can be recognized where the standard error depends linearly on time. This is not in accordance with the formula found earlier, but not enough can be said because of the lack of many measurements. A faster simulation algorithm is required.

4.2. Simulating photon arrivals directly using the exponential distribution

Photons arriving at a surface follow a Poisson distribution. Given a Poissonian event, the time to the next event can be described by an exponential random variable. By simulating the time until the next event, all bins inbetween can be skipped. This reduces the computation complexity by several orders of magnitude, as the photon rate is in the order of 1×10^7 whereas there are 1×10^{12} bins per second for the system defined in table 4.1.

The exponential distribution does assume that the photon rate of arrival is constant. If the laser is assumed to be a block pulse, this holds true only for very short intervals of $\frac{T_L}{2}$. This presents a problem, as the boundaries between the many intervals of signal or no signal are hard to frame.

Solving this problem is straightforward for a block wave but more difficult for a sine wave. In the former case, random number generation can be split into two distributions, one for ambient and one for laser light. They are both assumed always-on, but for the laser case a check is used to see whether the laser would have been on in that instant (and thus, whether the photon could arrive). If it would not have been, the photon is ignored. This way, the distribution still holds as new photons arrive some time after the previous photon, but afterwards in post-processing, photons which could not have arrived are stripped.

While this allows several orders of magnitude longer simulations, this is not enough yet for the type of low SNR simulations that represent real-life scenarios. Furthermore, non-block waves cannot be simulated since the photon arrival distribution changes continuously over time. This simulation abuses the fact that a block wave consists of only two values, one of which is zero.

Because of this, another simulation was created that does not simulate individual photons, or individual bins, but directly simulates the histogram.

4.3. Simulating noise and signal photon counts using a normal distribution

The former two simulators were created while figuring out the mathematics behind all processes at play. This is the reason only block waves are supported. The simulator presented in this section does support arbitrary waveforms. It also supports breaking a measurement into arbitrarily small subintervals and an arbitrarily worse resolution of the TDC.

The simulator, written in Rust, is built up as follows. First, the simulator is configured by creating a data structure called `System`. This data structure contains parameters for all base components:

- The laser, defined by its optical power output, the wavelength and pulse frequency;
- The SPAD, defined by its radius, field of view, dead time and P_{pd};
- The number of SPADs in use;
- The bandwidth of the optical filter in use before the SPAD;
- The TDC, defined by its resolution;
- The resolution that should be obtained, i.e. the amount of bits that should be gained over the pre-processed TDC output;
- The target, defined by its reflectance and distance;
- The ambient light intensity in kilolux;
- The number of subintervals per measurement;
- The total observation interval T_{obs};
- The waveform emitted by the laser;
- The waveform used for correlation.

There are now 2 resolutions of the TDC: the actual resolution of the physical device τ_{tdc} and the desired resolution after post-processing τ_{meas}. The desired resolution should be an integer multiple of the actual resolution, since no parts of bins can be simulated.

Before starting the measurement, some initialization is needed:

For every `System` run, two average photon detection rates are calculated using the formula from section 3.1. The number of bins for every subinterval B_a is calculated, as well as the wanted bin count

B_w:

$$B_a = \frac{T_L}{\tau_{\text{tdc}}} \tag{4.5}$$

$$B_w = \frac{T_L}{\tau_{\text{meas}}} \tag{4.6}$$

The laser waveform is generated, sampled to B_w bins, and each element multiplied with R_{laser}. The maximum amplitude before multiplication depends on the exact waveform, as the power contained in the waveform needs to equal 1 W (the power is already taken into account in R_{laser}). The number of SPADs as well as the observation interval T_{obs} are also taken into account here.

Then, to introduce the noise discussed in section 3.6.2, the created waveform is cyclically shifted by a random offset smaller than 1 LSB = $\frac{B_w}{B_a}$. Afterwards, the shifted waveform is downsampled to B_a bins. This waveform is used to create an array of normally distributed random variables, where the mean of the variables is given by the waveform and the variance is given by the ambient light, as described in eq. (3.24).

Subintervals are simulated by sampling the random variables, correlating this with the waveform specified in the `System` and finding the maximum of this correlation. Then, the results of these subintervals need to be combined. However, mere averaging does not work as shown in fig. 4.4.

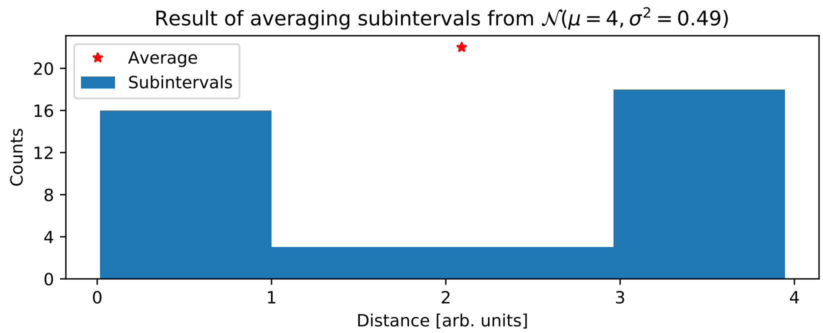

Figure 4.4: Why results of subintervals need to be combined in a smarter way than by averaging

Before the results can be combined, we need to find out in what quadrant most results are. In fig. 4.4, given a true distance of 4, the most likely subinterval results are the lowest and the highest bin. Averaging would end up somewhere in the middle, which gives the maximum possible error even though the subintervals have a small error. This needs to be taken into account before averaging the results from the subintervals.

4.3.1. Finding and exploiting available parallelism

Measuring each subinterval then consists of sampling each random variable in this array, performing the correlation and finding the maximum. Since the subintervals are uncorrelated, sampling and performing the correlations can be done in parallel. Furthermore, in order to estimate the standard deviation, the same scenario should be simulated often. This can be done in parallel too. Lastly, different points of interest can be analyzed in parallel as well. Given that a graph consists of dozens to hundreds of datapoints, around a thousand simulations are needed to estimate the standard deviation decently, and each run consists of dozens to thousands of subintervals, this application has a lot of parallelism. Furthermore, performing a correlation consists of an FMA operation of N numbers with N cyclically shifted numbers. Here, too, parallelism is found.

This parallelism can be exploited in several ways. The deepest form, of performing a correlation in parallel, is done by means of SIMD instructions [81]. All other parallel possibilities are exploited by putting all tasks in a threadpool. From this threadpool, several workers pull tasks and execute them. In this sense, all available parallelism is used.

Massively parallel devices

The simulator is an inherently easily parallelizable program. The question arises whether devices exist that are more easily able to extract this high level of parallelism, as when simulating often tens of thousands of tasks are spawned. A GPU is an obvious solution to this problem, as using GPGPU thousands of cores can be programmed. However, the current state of the art in GPGPU means that it is still a hassle to program code for these devices. Using toolchains such as CUDA [82] and OpenCL [83], it is a bit easier to manage, but it is still a lot of work.

Other options are ASICs, which is discarded immediately because of its expensive character, and programming an FPGA. Just like the GPU, an FPGA also appeared to be too much work, especially because of the desire to implement the algorithm itself, using a real SPAD and laser, on an FPGA. This is why only the parallelism of the CPU was exploited in the simulator.

4.4. Results

The simulator is used to confirm several types of relationships. Since the simulator works by generating the amount of photons in a bin directly, some aspects cannot be simulated. The effect of more SPADs, or a longer measurement time, for instance, both translate directly to a higher simulated bin count. The effects of these cannot be studied separately using this simulator, as these effects are canceled before the simulation starts. Furthermore, this simulator does not support multiple SPADs in any k-of-N trigger scheme.

To start with, the simulated and calculated rates for the system of table 4.2 are shown in fig. 4.5. The parameters are unrealistic. The sunlight intensity used is that of maximum intensity as calculated in section 3.1. The SPAD radius used is what is currently available for testing purposes. Other parameters are taken at sensible values, except for the observation time. The observation time is varied between unrealistic boundaries to allow the system behavior to be shown at both low-SNR and high-SNR scenarios. For all results, all parameters are equal to those specified in table 4.2 except those named specifically.

Table 4.2: Default system simulated

Laser pulse frequency	1×10^{8} Hz
Dead time	5×10^{-9} s
Number of SPADs	1024
Measurement resolution τ_{meas}	$9.765\,625 \times 10^{-12}$ s
TDC resolution reduction factor L	1
Subintervals M	1
Target reflectivity χ_R	0.4
Laser intensity waveform	sine
Correlation waveform	sine
T_{obs}	1×10^{-7} s to 1×10^{-4} s

The simulated and calculated standard error follow each other well, except for the beginning and near the end. This is caused by the maximum average standard deviation being limited to a quarter of the full dynamic range. Because this limitation is not taken into account in the formula for standard deviation used, the graph will deviate slightly. Near the bottom end of the graph, a slight deviation from the calculated error appears. This is due to the effects shown in fig. 3.21 in combination with an imperfect simulated distance.

Figure 4.5 shows that eq. (3.39) is correct. Now, if a TDC is used with poorer resolution, the error will increase. The error is shown in Bins as well as meters. If a TDC is used with lower resolution than the system described in table 4.2, bins refers to the original resolution.

If the resolution of the TDC is made poorer, the noise floor will be reached sooner. Figure 4.6 shows these results. The simulated and calculated standard errors are shown on top of each other.

A system where the TDC has lower resolution results in higher errors. As explained in section 3.6, the original error can be achieved by introducing subintervals. This is shown in fig. 4.7. Figure 4.8 shows system behavior when M, the amount of subintervals, is equal to the square of the drop in resolution, L. It is shown that the same noise floor can be reached, but only after a certain SNR is reached. If the observation time is smaller, the result is substantially worse than when less subintervals are used. This is due to the effect described in fig. 3.22, that the result of the measurement is nearly uniformly distributed.

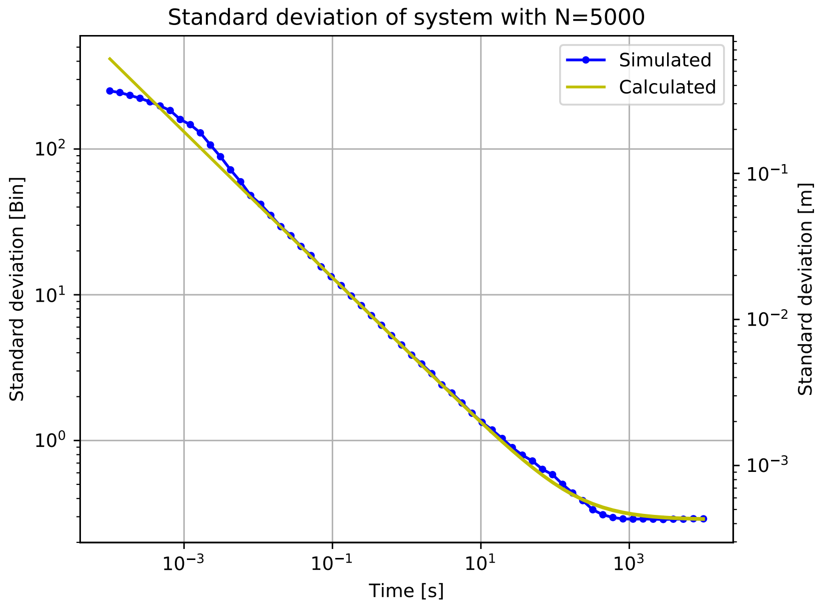

Figure 4.5: Simulated and calculated standard deviation over time for the base system. On the left side, the observation time is so low that the error is equal to its maximum value. On the right, the right bin is always selected. However, the actual distance is not an integer, and the error floor is thus a fraction of one bin

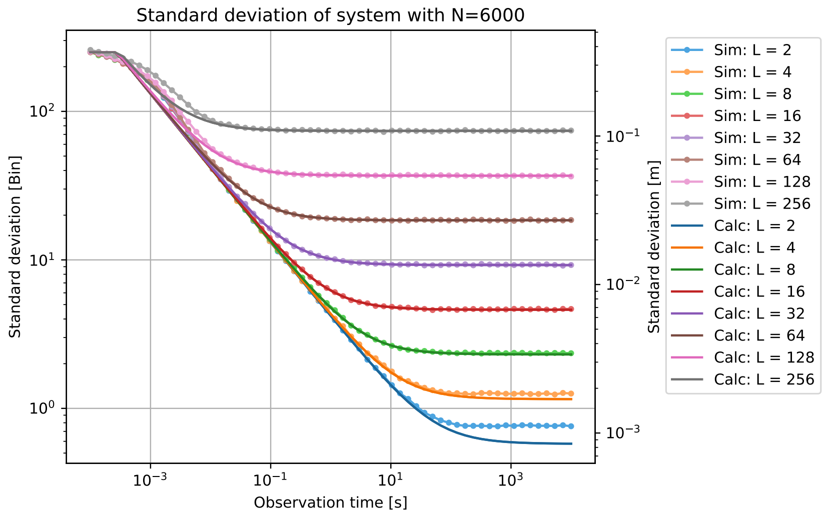

Figure 4.6: Simulated and calculated standard deviation over time, shown for different resolutions. Where before the maximum error was a fraction of one bin, using wider bins means that, in terms of the original system, the error may be larger than a single bin.

Figure 4.9 shows what happens when the noise described in fig. 3.21 is not introduced. At the correct SNR, the noise floor is reached, but quickly afterwards the standard error increases again.

Figure 4.10 shows the behavior of the system when the opening angle is increased. The combined effects of less signal and more noise are clearly visible: a large opening angle reduces system performance.

For different waveforms, fig. 4.11 shows the effect of the laser waveform, like in fig. 3.18. In this case, the laser and correlation waveforms are kept equal, but both are changed. A pure block pulse changes the slope of the detection. As the laser waveform approaches a block pulse, performance is a constant factor better than a sine pulse. No mathematical analysis is available for non-sine waveforms, as discussed in section 3.5.

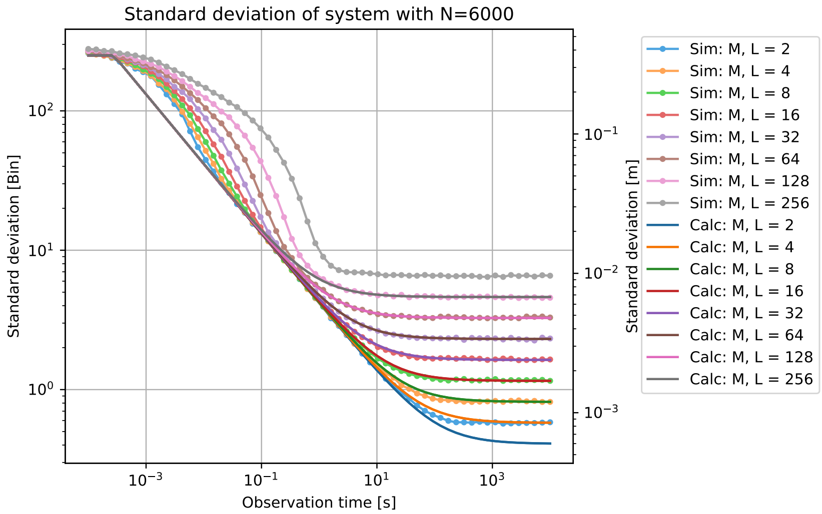

Figure 4.7: Simulated and calculated standard deviation over time, when varying L, the TDC resolution reduction factor, and M, the amount of subintervals per measurement simultaneously. Observed are the noise floors, which, although less pronounced than in fig. 4.6, still rise with L and M.

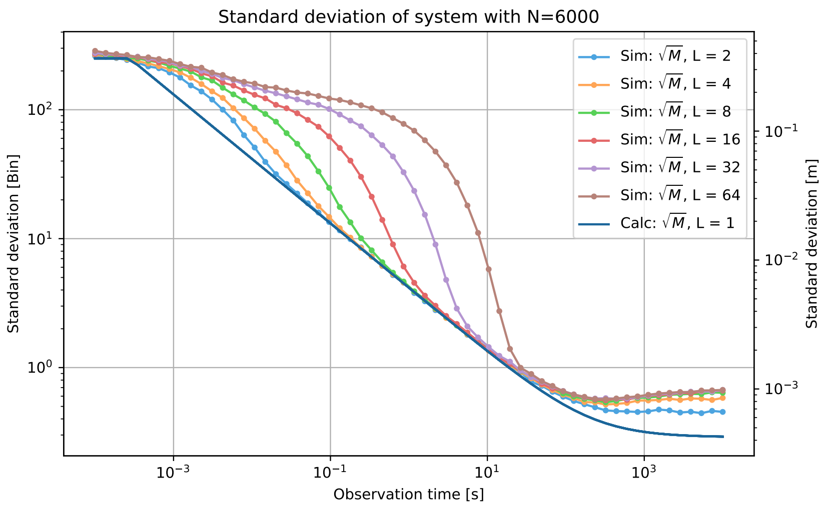

Figure 4.8: Simulated and calculated standard deviation over time, when varying L and varying M squared. The noise floors are finally comparable, but the observation time needed to reach this noise floor does increase. This is caused by the effect described in fig. 3.22, that the result of the subinterval approaches a uniform variable. As the (wrapped) tail becomes smaller, the result of the measurement quickly approaches the noise floor.

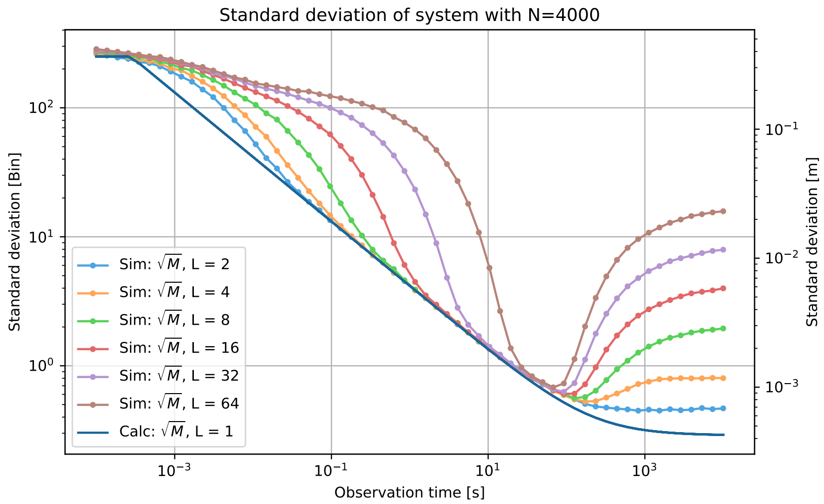

Figure 4.9: Simulated and calculated standard deviation over time, when varying L and varying M squared, but without introducing any noise. The noise floor is reached, but because of the effects described in fig. 3.21, the noise rises when the the observation time increases beyond this point.

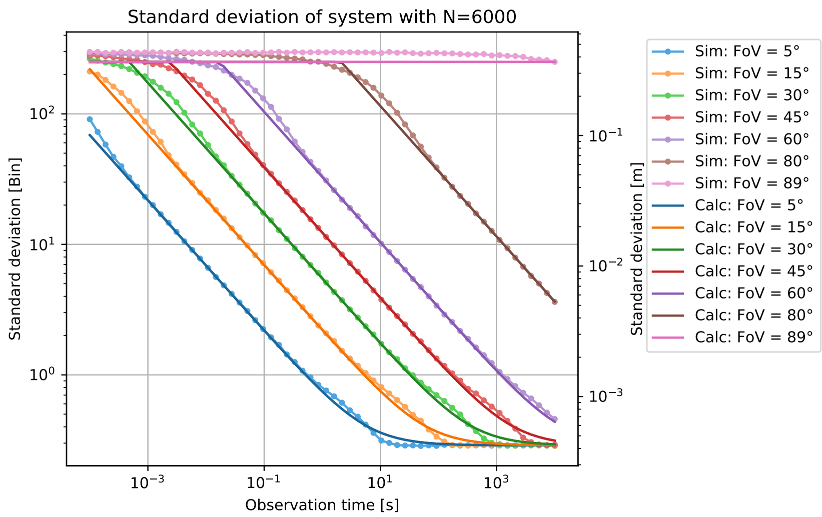

Figure 4.10: Simulated and calculated standard deviation over time, when varying the field of view of the SPAD and laser. This means that for large opening angles, most of the power is at the edge of the circle, reducing the amount of returning power.

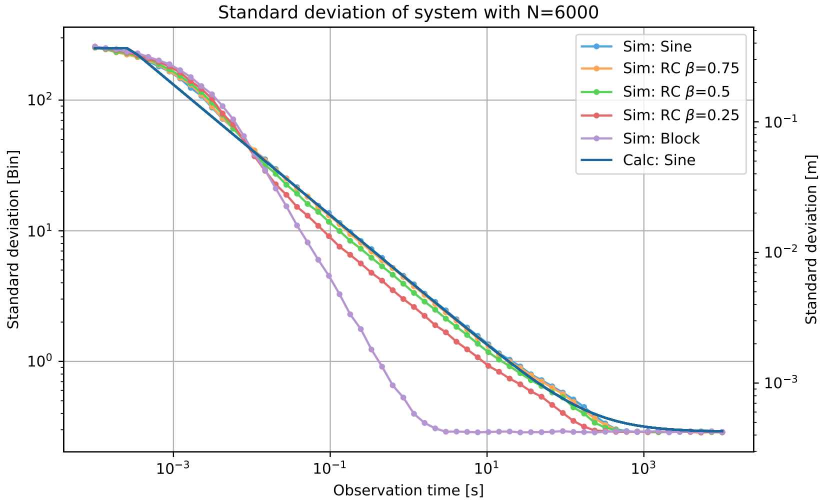

Figure 4.11: Simulated and calculated standard deviation over time, for different waveforms. Only for the pure sine does the mathematical formula provide an answer. For a block pulse, the slope of the graph is completely different. For any other wave, a gain of a constant factor applies.

5 Conclusion

In this thesis, time of flight with light using single-photon avalanche diodes (SPADs) has been analyzed.

An analysis of the state of the art was performed where different detection methods were investigated. After validating the choice of time-of-flight using SPADs, two main design problems were identified: detecting single photons and measuring tiny time differences.

To this end, the physics of SPADs, one type of single-photon detector, were analyzed. Specifically, behavior in saturation was analyzed as in the target application high ambient photon rates can be expected. In near-infrared, photon detection with silicon is more complicated, leading to photon detection probabilities in the order of 1 % to 2 %.

Next, the problem of time discretization was tackled. Many different time discretization architectures exist. A resolution better than the switching time of single transistors can be obtained. However, this costs area and energy. The read-out time quickly increases as well. Thus, using a simple counter is preferable, if possible.

A mathematical analysis of the system was performed. Typical returning photon rates were calculated, as well as typical ambient photon rates. The latter is often multiple orders of magnitude larger than the former. A method was described that uses the time difference between the start of the laser pulse and the arrival of photons to estimate distance.

The effect of different waveforms was analyzed, both for the laser and for the correlation. As long as the correlation waveform is a sine, the exact laser waveform is less of a concern. However, lasers emitting square waves can achieve much better performance (but are more difficult to create).

Different combinations of multiple SPADs were investigated. There are better methods than the trivial solution: adding the arrival times of all photons to a single histogram. However, these methods only make sense beyond tens of thousands of SPADs and perform much worse for only tens or hundreds of SPADs.

Lastly, the effect of lowering the resolution of the TDC was investigated. A trade-off appeared feasible where, at the cost of slightly higher computational complexity, the same resolution can be obtained using a lower resolution TDC by averaging the results from several subintervals. This would allow simple TDCs to be used while still achieving the desired resolution.

A formula is found for the standard error of the whole system, shown in eq. (5.1).

The results of this simulation are confirmed by simulation using multiple simulators. One simulator was built that simulates single photons. This simulator confirmed the saturation effects. Another simulator was used that directly simulates histograms to analyze the detection method. The simulator shows that the same noise floor can be reached by choosing M equal to L^2. The effects of leaving out quantization noise are shown, where the standard error rises again after reaching the noise floor. Lastly, the simulation also shows the effects of different waveforms, such as sine waves, square waves, and raised cosines.

5.1. Answers to research questions

Question 1: What are trade-offs found in current state of the art proximity sensing devices?

In current state of the art distance measurement devices, many trade-offs exist. Power consumption, maximum range, resolution, refresh rate, SPAD area, and ambient noise (in the form of light or sound) tolerance are directly interchangeable. This can be seen in table 2.1, where several solutions are shown that trade these properties. Several low-power products exist, but their range is limited. Several solutions have a high ambient light tolerance, but their range is limited. One sensor has a high resolution, but the maximum range is low, and its power consumption is high.

Question 2: In what area does time-of-flight technology shine?

Time-of-flight technology does not require two parts placed at distinct locations, unlike position-sensing devices. However, position-sensing devices can obtain higher accuracy than time-of-flight-based devices. Unlike ultrasound technology, there are no resonance effects limiting detection in the low range. Unlike intensity-based solutions, time-of-flight technology is insensitive to the reflectivity of the target, increasing accuracy. Ultrasound devices, as well as position-sensing devices, cannot be integrated into a single package.

Time-of-flight technology is well suited to applications that require a small sensor, low power consumption, do not require a long range, require high accuracy and medium resolution.

Question 3: What are the typical worst-case signal and noise conditions for such a system?

Using the SMARTS model, typical ambient light conditions were calculated. Given a 40 nm bandwidth around 940 nm and excluding direct sunlight, about 0.35 W m^{-2} hits a surface in worst-case conditions. The worst-case conditions used were noon in the summer on a cloudless day, approximately 23° north of the equator. For laser light, an analysis was performed in section 3.1.1, resulting in a formula that takes all parameters into account. The photon return rate depends on:

- The power transmitted by the laser;
- The distance to the target
- The reflectivity of the target;
- The opening angle of the SPAD and the laser;
- The area of the SPAD;
- The photon detection probability of the SPAD;

Given a typical scenario, about 1×10^3 photons per second arrive at the SPAD due to the laser, whereas about 1×10^5 photons per second arrive at the SPAD due to ambient noise.

Question 4: How well does such a system perform, what is the standard deviation of the measurement?

The following formula is found for the standard error of the whole system:

$$\sigma_\text{m} = \sqrt{\frac{c^2 \cdot L^2 \cdot \tau_\text{desired}^2}{48M} + \left(\frac{c}{2} \sqrt{\frac{hc}{\lambda}} \frac{T_\text{laser} \cdot d^2}{\sqrt{T_\text{obs} N_\text{SPAD} \pi r_\text{spad}^2 P_{pd}}} \frac{\theta}{\cos^2(\theta)\, \chi_\text{R}} \frac{\sqrt{I_\text{a}}}{P_\text{t}} \right)^2} \tag{5.1}$$

In this formula, c is the speed of light in vacuum, L the resolution of the TDC divided by the desired measurement resolution, τ_desired the desired measurement resolution, h the Planck constant, M the number of subintervals per measurement, λ the wavelength of the laser, T_laser the oscillation frequency of the laser, d the distance of the target, θ the opening angle of both SPAD and laser, T_obs the total observation interval, I_a the ambient light intensity, P_t the transmission power of the laser, N_SPAD the number of SPADs used in the measurement, r_spad the radius of a single SPAD and χ_R the reflectivity of the target.

The standard deviation of the measurement error of the system depends on many factors. In chapter 4, the standard deviation is shown for many systems. The formula for standard deviation found in eq. (3.27) is confirmed by simulation. System performance depends on the photon arrival rates due to the laser and ambient noise, and on:

- The pulse frequency of the laser;
- The observation time;
- The resolution of the used TDC;
- The number of subintervals per measurement.

Several interesting relations are verified using the simulator.

5.2. Future work

Many aspects of proximity sensing are left out of scope of this thesis.

- Acoustic sensors were not considered. In high-ambient-light scenarios, they may provide superior solutions. However, care should be taken that the environment is not disturbed when using acoustic sensors, as sound travels further than light.
- System behavior when more realistic waveforms are used. Square waves, sines, and all sorts of raised-cosines were looked at. When using a sine wave for the correlation, the exact waveform is less relevant. However, more RC-like waveforms were not considered. From the square wave, the sine, and the raised cosines, we can conclude that slight deformations of the waveform only have small effects.
  The achievable gains for an equal laser and correlation waveform in RC-like scenarios are interesting to look at, especially as lasers themselves are imperfect. What can be gained by accurately measuring the waveform and using that for correlation?
- Using a SPAD, a laser, and an FPGA, the system can be tested in a real-life environment. This requires the implementation of a low-resolution TDC and the full correlation algorithm.
- Designing an actual system on a chip. Here, the trade-offs between more SPADs, more TDCs and a parallel or sequential correlation algorithm become relevant.
- Analyze other applications for this system. For instance, currently, state of the art cameras use images to focus the camera. Time-of-flight may provide alternative solutions.

A

Distributions

A.1. Poisson

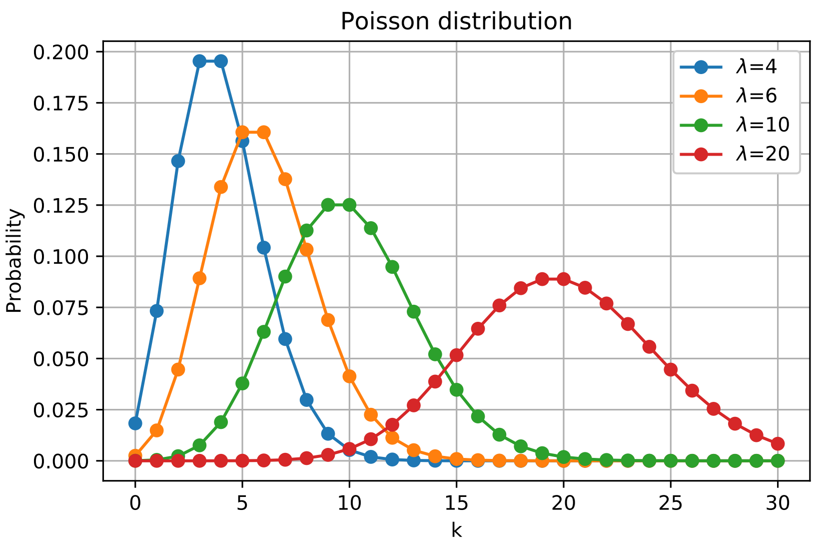

Figure A.1: Poisson distribution for different λ

A.2. Normal

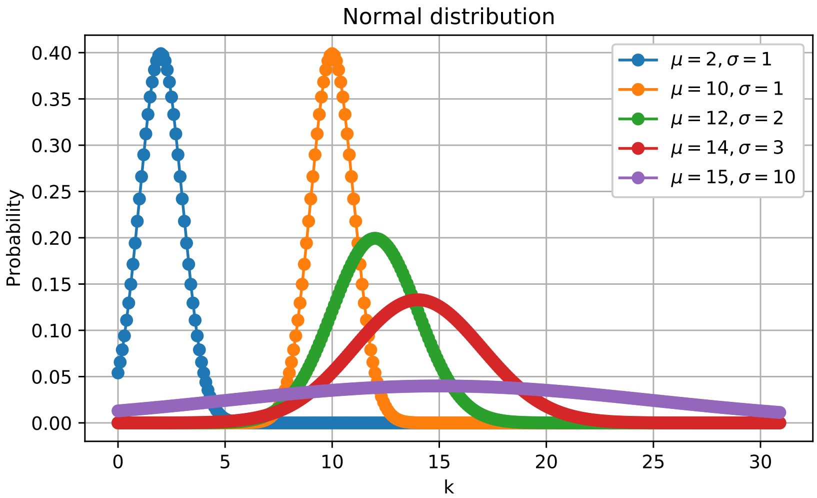

Figure A.2: Normal distribution for different μ and σ

A.3. Binomial

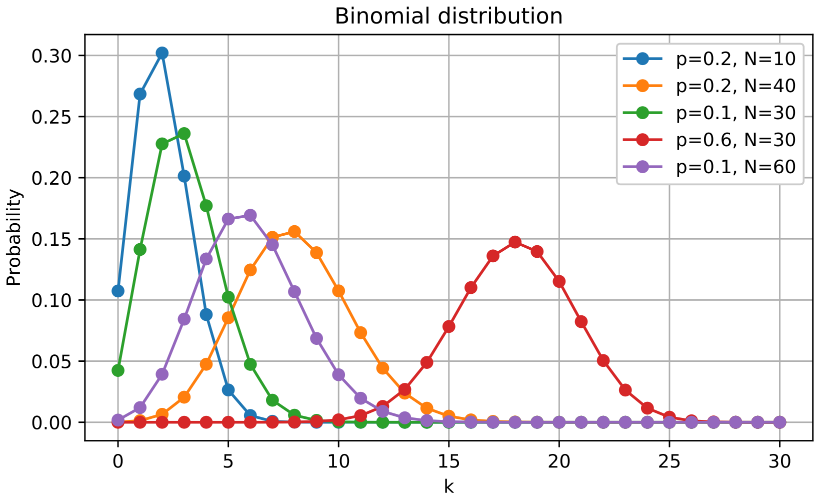

Figure A.3: Binomial distribution for different p, k, N

B

Reflection analysis

This appendix contains an analysis of different approaches to surface reflection related to human skin, which result in the conclusion that it is not possible to catch reflectance of humans in typical usage scenarios in a simple formula. Because of this, the assumption is made that typical reflectance is about 0.4. The accuracy of this assumption is sometimes low, but it is the best that can be done.

Optical view of reflectance

Reflectance in general is due to two physical phenomen

- Specular, due to the Fresnel effect [84],
- Diffuse, due to subsurface scattering.

The specular reflection is mainly due to the upper layer of the skin, called sebum. The diffuse reflection is due to the epidermis and the dermis.

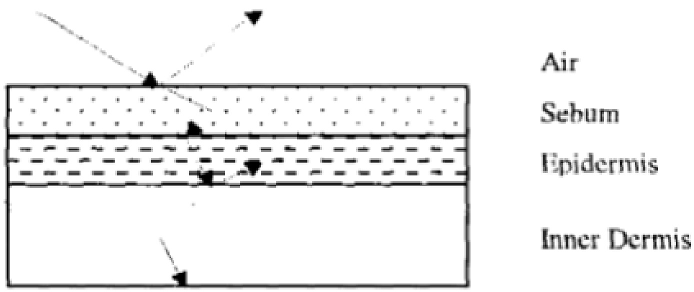

Figure B.1: Light propagation in a three-layer skin model[84, 85]

Skin reflectance has typically been modelled by a constant Lambertian term. However, as shown by [84], the high amount of water in skin causes a directionally varying component. Diffuse reflectance dominates at lower incident angles, whereas specular reflectance dominates at higher angles of incidence.

An experiment was done by CUReT (Columbia-Utrecht Reflectance and Texture database), which can be found at `http://www1.cs.columbia.edu/CAVE//exclude/curet/.index.html`. They took 61 different materials, among which a piece of human skin, seperated from a dead body, and measured the BRDF (Bidirectional reflectance distribution function) [86]. This is based on the Oren-Nayar model [87, 88]. The result of the BRDF is the amount of light being returned, as a function of the incoming light direction (both azimuth and zenith angle) and the outgoing light direction. For many angles, the reflectance was measured for 205 distinct angles.

Several questions now arise. There is a difference between the reflectance of dead human skin and that of a live human, and perhaps more importantly, reflectance of humans also depends on clothing, and that depends on folds, material, color, wetness, etc. Clearly, it would go far beyond the scope of

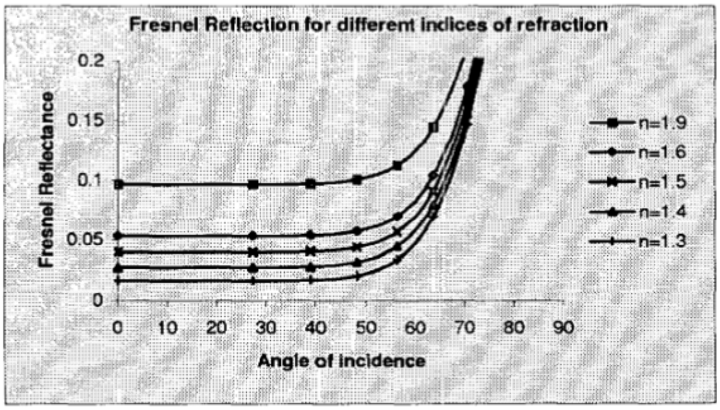

Figure B.2: Effect of refrective index n on Fresnel reflectance [84]

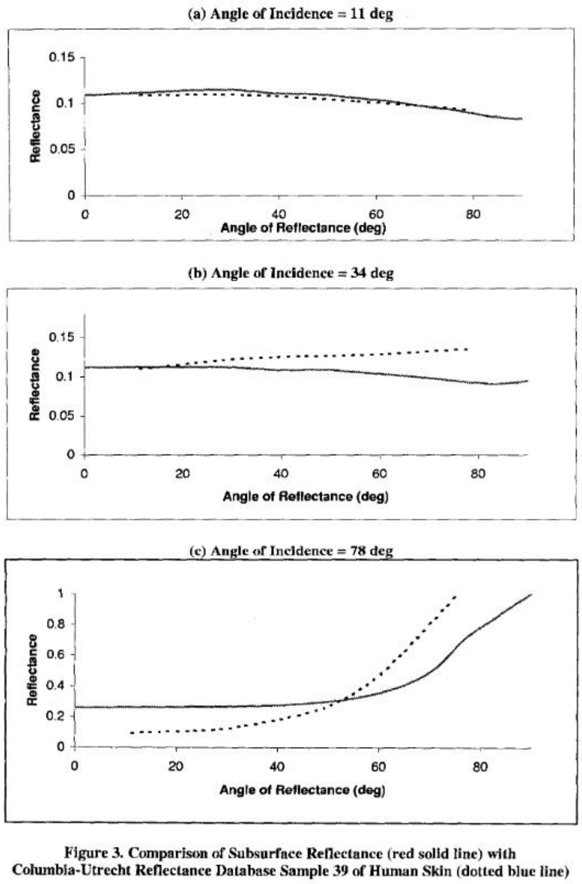

Figure B.3: Comparison of subsurface reflectance (solid line) with CUReT database

this work to analyze all of this. This is not necessary either, since these aspects are mostly only relevant for machine vision applications.

For this use case, it suffices to say that reflectance of humans depends on many factors and because of this, an approximation that holds in most cases cannot be created. Thus, the reflectance of the infinite wall of skin is used, because this takes the effect of an increasing field of view into account as well as the increasing distance.

C

Signal return rate calculation

The formula for signal return power given a nonzero field of view of the SPAD and laser is not trivial. This appendix contains this derivation. The starting point is the analysis done in section 3.1.1. The type of surface is taken into account, and a surface integral is solved for the projected surface on the wall. This leads to a slightly adjusted formula, which contains two cosines more than the non-field-of-view version.

Let us assume that the SPAD and VCSEL have the same field of view. Then, all signal light is projected onto a virtual wall (that has the reflectivity of human skin) From each point on this circle on the wall, light returns in a hemisphere. The fraction of light that is received is given by the area of the SPAD projected onto this hemisphere, divided by the size of this hemisphere. It is assumed the surface is Lambertian, which means that the intensity of the returned power follows the cosine of the angle of reflectance. Because the SPAD is a projection onto this hemisphere, the effective area of the SPAD is smaller as the angle gets larger, following the cosine as well. The surface integral over this circle on the wall then gives us:

$$P_r = \int_0^{2\pi} \int_0^{R} \frac{P_t}{A_{\text{wall}}} \cdot \chi_{\text{R}} \cdot \cos^2(\theta) \cdot \frac{A_{\text{spad}}}{A_{\text{hemisphere}}} \cdot r \, \mathrm{d}r \, \mathrm{d}\phi \tag{C.1}$$

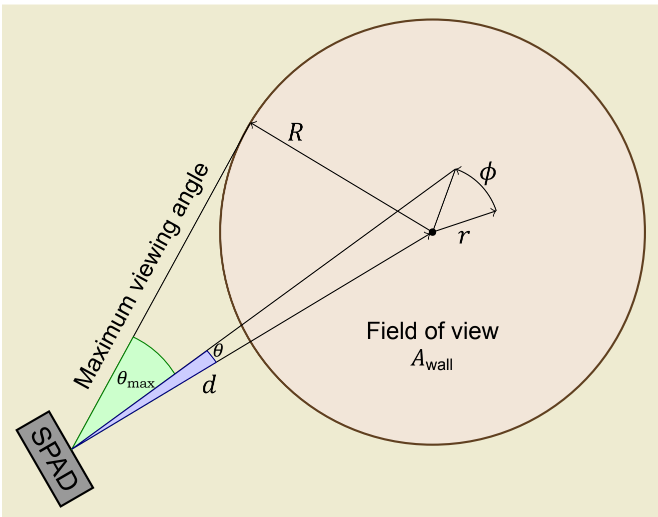

Figure C.1: Light reflecting off of a wall, back view

In this equation, χ_{R} is the reflectivity of the wall, θ is, for a given point on the circle, the angle between two lines; one going from that point to the SPAD, and the other from the SPAD to the middle of the circle. The maximum angle here is given by the field of view. ϕ is part of the surface integral, however because

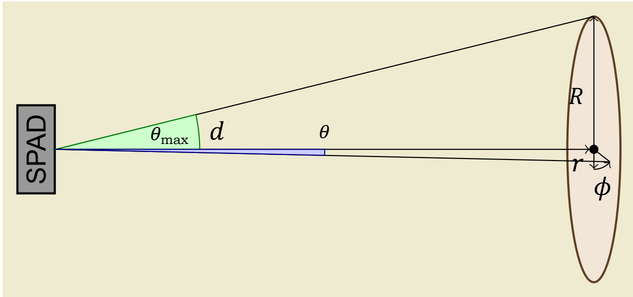

Figure C.2: Light reflecting of a wall, side view

there is no variation in this dimension it can be solved and replaced by 2π immediately. The wall area A_{wall} is the area of the wall that is illuminated. The assumption is made that the power per unit area is equal throughout this surface.
Also, we can rewrite θ as the inverse tangent of the opposite edge (r) over the adjacent edge (d); this way we express θ in terms of r, which is the integrand. Furthermore, the distance from a point to the SPAD is given by Pythagoras given the radius of the circle (r) and the distance between the midpoint and the SPAD (d). The area of the wall that is illuminated is equal to πR^2. Thus, the integral reduces to:

$$P_r = 2\pi \int_0^R \frac{P_t}{\pi R^2} \cdot \chi_{\text{R}} \cdot \cos^2\left(\arctan\left(\frac{r}{d}\right)\right) \cdot \frac{A_{\text{spad}}}{2\pi\,(r^2+d^2)} r \, \mathrm{d}r$$

Furthermore, R is the maximum radius of the circle, which is equal to the field of view at the maximum distance, or

$$R = \tan(\theta_{\max}) \cdot d$$

Here θ_{max} is half of the Field of View. The integral now contains many constants, and can be simplified:

$$P_r = P_t \chi_{\text{R}} A_{\text{spad}} \frac{1}{\pi} \int_0^{\tan(\theta_{\max})\cdot d} \frac{r\cos^2\left(\arctan\left(\frac{r}{d}\right)\right)}{(r^2+d^2)\left(\tan(\theta_{max})\cdot d\right)^2} \, \mathrm{d}r$$

Now, the cosine of the arctangent can be replaced because:

$$\cos(\arctan(x)) == \frac{1}{\sqrt{x^2+1}}$$

And because

$$\left(\frac{r^2}{d^2}+1\right)^2 \cdot d^2 = r^2 + d^2$$

We obtain:

$$P_r = P_t \chi_{\text{R}} A_{\text{spad}} \frac{1}{\pi} \int_0^{\tan(\theta_{\max})d} \frac{r}{(r^2+d^2)^2 \tan^2(\theta_{\max})}$$

Evaluating the integral gives, as specified in [71]:

$$P_r = \frac{P_t \chi_{\text{R}} A_{\text{spad}} \cos^2(\theta)}{2\pi d^2}$$

The energy contained by a single photon can be calculated given only its wavelength, using the speed of light and the Planck constant:

$$E_{\text{photon}} = \frac{h \cdot c}{\lambda}$$

And given a photon detection probability, which is an aspect of the SPAD and depends on the wavelength, we obtain a rate of photons per second:

$$R_{\text{photons}} = P_r \cdot \frac{1}{E_{\text{photon}}} \cdot P_{\text{pd}}$$

$$R_{\text{photons}} = \frac{P_t \chi_{\mathrm{R}} A_{\text{spad}} \cos^2(\theta)}{2\pi d^2} \frac{P_{pd}}{E_{\text{photon}}} \tag{C.2}$$

As expected, the photon return rate is dependent on the square of the distance.

Given a transmission power P_t of 2 mW, a reflectivity of 0.4, a SPAD radius r_{spad} of 29.3 μm, a $\theta_{\max}$ of 25°, a P_{pd} of 0.01, a target distance d and a photon energy of 2.11×10^{-19} J, the received signal power is 3.377×10^{-13} W and the photon rate is approximately $1.6 \times 10^4\ \mathrm{s}^{-1}$.

D

SMARTS Parameters

The Simple Model of Atmospheric Radiative Transfer of Sunshine, or SMARTS[1] model, originally created in 1995, tries to model solar activity. It can output solar intensity due to direct or indirect sunlight at almost any given place on earth. Because the product should function all over the globe, the worst conditions with respect to sunlight are taken into account. Given that the worst-case light intensity will occur at noon on a summer near the equator, the model is run with these (and more) parameters. The exact parameters used are noted in table D.1.

Table D.1: Parameters used by SMARTS model

Pressure	1.013 25 bar
Altitude	0 m
Height above ground	0 m
Atmosphere	sub-tropical summer
Water vapor data	Internal default
Ozone abundance input	Internal default
Gaseous absorption & pollution	Internal default
Carbon dioxide concentration	410 ppm [89]
Extraterrestrial spectrum	Gueymard 2004[90]
Aerosol model	Shettle & Fenn 1979[91], rural model
Turbidity data	$\tau = 0.084$
Zonal albedo model	Light soil (non-Lambertian)
Surface tilt	0
Inspected variables	Direct normal & diffuse horizontal irradiance

All of these parameters are taken at expected worst-case scenarios. The irradiance is calculated in a sub-tropical area, on the ground, at nominal pressure, during the summer. Furthermore, solar spectra are available from several scientific sources, the default was selected, as well as for many other parameters. The carbon dioxide concentration is explicitly updated because the used value was slightly outdated, as in the last few years the carbon dioxide concentration has changed significantly[89].

This model then calculates many irradiances at many frequencies. However, as specified previously, the bandwidth is constrained to the 920 nm to 960 nm range. Because of an absorption peak in the spectrum of water, and our atmosphere containing a lot of water, a large fraction of sunlight will be blocked before reaching the SPAD.

D.1. Sunlight intensities obtained from SMARTS model

The following two intensities are obtained from the model, due to direct sunlight:

$$P_{\text{direct, 920 nm to 960 nm}} = 11.595\,\mathrm{W\,m^{-2}} \tag{D.1}$$

$$P_{\text{diffuse, 920 nm to 960 nm}} = 0.351\,\mathrm{W\,m^{-2}} \tag{D.2}$$

Bibliography

[1] C. A. Gueymard, “Smarts2: A simple model of atmospheric radiative transfer of sunshine,” Florida Solar Energy Center, Tech. Rep., 2006, [Originally published in 1995].

[2] E. Towe, R. F. Leheny, and A. Yang, “A historical perspective of the development of the vertical-cavity surface-emitting laser,” *IEEE Journal of Selected Topics in Quantum Electronics*, vol. 6, no. 6, pp. 1458–1464, Nov 2000.

[3] R. Semiconductor, “Ambient light sensor (als) applications in portable electronics,” https://www.rohm.com/documents/11308/12928/CNA09016_wp.pdf, 2009, [Online; accessed 14-11-2019].

[4] M. Carbone, “Influence of temperature control limits on passively cooled computing system performance,” in *2015 31st Thermal Measurement, Modeling Management Symposium (SEMI-THERM)*, March 2015, pp. 41–45.

[5] I. Pires, N. Garcia, N. Pombo, F. Flórez-Revuelta, and S. Spinsante, “Approach for the development of a framework for the identification of activities of daily living using sensors in mobile devices,” *Sensors*, vol. 18, p. 640, 02 2018.

[6] P. Daponte, L. D. Vito, F. Picariello, and M. Riccio, “State of the art and future developments of measurement applications on smartphones,” *Measurement*, vol. 46, no. 9, pp. 3291 – 3307, 2013. [Online]. Available: http://www.sciencedirect.com/science/article/pii/S026322411300198X

[7] T. S. T. Lynda v. Mapes, “The Roar Below, How our noise is hurting orcas’ search for salmon,” https://projects.seattletimes.com/2019/hostile-waters-orcas-noise/, [Online; accessed 04-12-2019].

[8] Mosquito, “Mosquito Werking & Veiligheid,” https://www.hangjongerenweg.nl/werking-veiligheid/, [Online; accessed 05-02-2019].

[9] Vanderbilt Environmental Health & Safety, “Laser Safety,” https://web.archive.org/web/20071225083035/http://www.safety.vanderbilt.edu/safety_links/laser.htm, [Online; accessed 05-02-2019].

[10] T. Kuroda, “CMOS design challenges to power wall,” *2001 International Microprocesses and Nanotechnology Conference, MNC 2001*, pp. 6–7, 2001.

[11] J. Martins, R. Reis, and J. Monteiro, “Capacitance and power modeling at logic-level,” 01 2000.

[12] Automation Insights. Photoelectric Basics - Distance Measuring. https://automation-insights.blog/2016/03/30/photoelectric-basics-distance-measuring/. [Online; accessed 18-11-2019].

[13] OMRON Industrial Automation. FAQ00320 for Photoelectric Sensors. https://www.ia.omron.com/support/faq/answer/include/faq00320/img/FAQ00320-1.jpg. [Online; accessed 12-03-2019].

[14] Panasonic. Laser Displacement Sensor - Displacement Sensors. https://www3.panasonic.biz/ac/ae/service/tech_support/fasys/tech_guide/measurement/laser/index.jsp. [Online; accessed 19-02-2019].

[15] Allied Electronics & Automation. About Ultrasonic Proximity Sensors. https://expert.alliedelec.com/sensing/about-ultrasonic-proximity-sensors/. [Online; accessed 18-11-2019].

[16] A. Bujnowski, K. Czuszynski, J. Ruminski, J. Wtorek, R. McCall, A. Popleteev, N. Louveton, and T. Engel, “Comparison of active proximity radars for the wearable devices,” in *2015 8th International Conference on Human System Interaction (HSI)*, June 2015, pp. 158–165.

[17] Digikey. Fundamentals of Distance Measurement and Gesture Recognition Using ToF Sensors. https://www.digikey.nl/en/articles/techzone/2018/nov/fundamentals-distance-measurement-gesture-recognition-tof-sensors. [Online; accessed 12-03-2019].

[18] Brunelco. Time of flight sensor (Time of flight). https://www.brunelco.nl/technieken/time-of-flight-sensor-time-of-flight/. [Online; accessed 28-11-2019].

[19] Edoardo Charbon, “Introduction to time-of-flight imaging,” , 2018, [Online; accessed 9-October-2019].

[20] STMicroelectronics, “VL53L1X Long distance ranging Time-of-Flight sensor based on ST FlightSense technology,” https://www.st.com/content/st_com/en/products/imaging-and-photonics-solutions/proximity-sensors/vl53l1x.html, [Online; accessed 19-02-2019].

[21] ——, “VL6180X Proximity Sensor, Gesture and ALS module,” https://www.st.com/content/st_com/en/products/imaging-and-photonics-solutions/proximity-sensors/vl6180x.html, [Online; accessed 19-02-2019].

[22] Sensopart, “FR 90 ILA Reflector Distance Sensor,” https://www.sensopart.com/jdownloads/Produktdetails/FR_90_ILA_e.pdf, [Online; accessed 19-02-2019].

[23] Baumer, “Multi-spot laser distance sensor,” https://www.baumer.com/dk/en/high-performance-laser-distance-sensors-mesax-om70/om70-x0500-hi0660-vi/p/26333, [Online; accessed 19-02-2019].

[24] TeraBee, “TeraRanger One,” http://www.terabee.com/wp-content/uploads/2017/09/TeraRanger-One-Specification-Sheet1-1.pdf, [Online; accessed 21-02-2019].

[25] ——, “TeraRanger Evo 600Hz,” https://www.terabee.com/wp-content/uploads/2018/09/TeraRanger-Evo-600Hz-Specification-sheet.pdf, [Online; accessed 21-02-2019].

[26] TeraBee, “TeraRanger Evo 3,” https://www.terabee.com/wp-content/uploads/2018/09/TeraRanger-Evo-3m-Specification-sheet.pdf, [Online; accessed 21-02-2019].

[27] ——, “TeraRanger Evo 60,” https://www.terabee.com/wp-content/uploads/2018/10/TeraRanger-Evo-60m-Specification-sheet.pdf, [Online; accessed 21-02-2019].

[28] Benewake, “TFmini Infrared Module,” https://cdn.sparkfun.com/assets/5/e/4/7/b/benewake-tfmini-datasheet.pdf, [Online; accessed 19-02-2019].

[29] Garmin, “LIDAR Lite v3HP,” https://cdn.sparkfun.com/assets/9/a/6/a/d/LIDAR_Lite_v3HP_Operation_Manual_and_Technical_Specifications.pdf, [Online; accessed 19-02-2019].

[30] LeddarTech, “Leddar Vu8 8-segment solid-state LiDAR Sensor Module,” https://leddartech.com/app/uploads/dlm_uploads/2017/12/Spec-Sheets-LeddarVu-12avril2018-ENG-web.pdf, [Online; accessed 19-02-2019].

[31] Seeedstudio, “Seeedstudio Grove - TF Mini LiDAR,” https://www.seeedstudio.com/Seeedstudio-Grove-TF-Mini-LiDAR-p-2996.html, [Online; accessed 21-02-2019].

[32] SLAMTEC, “RPLIDAR A3 Low-Cost 360 Degree Laser Range Scanner,” https://www.generationrobots.com/media/LD310_SLAMTEC_rplidar_datasheet_A3M1_v1.0_en.pdf, [Online; accessed 19-02-2019].

[33] S. Partners, “Laser Distance Meter LAM51/52/53,” http://downloads.sensorpartners.com/datasheet-sensor-partners-LAM50.pdf, [Online; accessed 19-02-2019].

[34] Scantron, “Laser distance measurement for online applications,” https://scantronltd.co.uk/wp-content/uploads/2018/03/Scantron_SLS_Data_Sheet.pdf, [Online; accessed 19-02-2019].

[35] Broadcom, “AFBR-S50MV85G Time-of-Flight Sensor Module for Distance and Motion Measurement,” http://www.farnell.com/datasheets/2723104.pdf, [Online; accessed 21-02-2019].

[36] Simblee, “Simblee RFD77402 IoT 3D ToF Sensor Module,” https://www.digikey.com/product-detail/en/rf-digital-corporation/RFD77402/1562-1040-1-ND/6589215, [Online; accessed 19-02-2019].

[37] Renesas, “ISL29501 Time of Flight Signal Processing IC,” https://www.renesas.com/us/en/products/sensors/proximity-sensors/light-to-digital-sensors/device/ISL29501.html, [Online; accessed 21-02-2019].

[38] Sharp, “GP2Y0A21YK General Purpose Type Distance Measuring Sensors,” https://www.sparkfun.com/datasheets/Components/GP2Y0A21YK.pdf, [Online; accessed 19-02-2019].

[39] Sensopart, “FR 55 RLAP Distance sensor with reflector for large distances,” https://www.sensopart.com/jdownloads/Produktdetails/FR_55-RLAP_e.pdf, [Online; accessed 19-02-2019].

[40] Melexis, “MLX75024 Time-of-Flight Sensor Array,” https://www.melexis.com/en/documents/documentation/datasheets/datasheet-mlx75024, [Online; accessed 21-02-2019].

[41] Baumer, "Laser distance sensor," http://vt.baumer.com/in-en/products/productfinder/?tx_baumerproductfinder_pf%5Burl%5D=%2Fpfinder_sensor%2Fscripts%2Fproduct.php%3Fcat%3DCONFMyAppli%26pid%3DOADM_260I1101_S14C%26language%3Den, [Online; accessed 19-02-2019].

[42] ——, "Ultrasone Sensor U500," https://www.baumer.com/ch/en/product-overview/distance-measurement/ultrasonic-distance-sensors/robust-ultrasonic-sensors-with-flexible-parameterization/c/medias/__secure__/Baumer_Ultrasonic_sensors_EN_20181025_BR_11208133.pdf?mediaPK=8933117722654, [Online; accessed 19-02-2019].

[43] Maxbotix, "HRLV MaxSonar High-Resolution, Precision, Low-Voltage Ultrasonic Rnage-Finder," https://www.maxbotix.com/documents/HRLV-MaxSonar-EZ_Datasheet.pdf, [Online; accessed 19-02-2019].

[44] Sensopart, "UM 18-60 Ultrasonic sensor with switching output," https://www.sensopart.com/jdownloads/Produktdetails/UM_18-60-250_e.pdf, [Online; accessed 19-02-2019].

[45] ——, "UMT 30-3400 Ultrasonic Sensor with switching output," https://www.sensopart.com/jdownloads/Produktdetails/UMT_30-3400_e.pdf, [Online; accessed 19-02-2019].

[46] M. Beer, J. Haase, J. Ruskowski, and R. Kokozinski, "Background light rejection in spad-based lidar sensors by adaptive photon coincidence detection," *Sensors*, vol. 18, p. 4338, 12 2018.

[47] E. Charbon and M. Fishburn, *Monolithic Single-Photon Avalanche Diodes: SPADs*, 08 2011, vol. 160, pp. 123–157.

[48] S. Burri, "Challenges and solutions to next-generation single-photon imagers," Ph.D. dissertation, Lausanne, 2016. [Online]. Available: http://infoscience.epfl.ch/record/220243

[49] J. M. Rabaey, A. Chandrakasan, and B. Nikolic, *Digital Integrated Circuits (2nd Edition)*. Pearson, 2003. [Online]. Available: https://www.amazon.com/Digital-Integrated-Circuits-2nd-Rabaey/dp/0130909963?SubscriptionId=AKIAIOBINVZYXZQZ2U3A{&}tag=chimbori05-20{&}linkCode=xm2{&}camp=2025{&}creative=165953{&}creativeASIN=0130909963

[50] J. Lu, B. Li, F. Yuan, and Y. Xu, "A compact spad pixel with active quenching and recharging," in *2019 China Semiconductor Technology International Conference (CSTIC)*, March 2019, pp. 1–3.

[51] L. Zheng, G. Zhang, J. Wu, H. Hu, and W. Sun, "Compact and rapid detection quenching circuit for spad arrays," in *2017 International Conference on Electron Devices and Solid-State Circuits (EDSSC)*, Oct 2017, pp. 1–2.

[52] F. Ceccarelli, G. Acconcia, A. Gulinatti, M. Ghioni, and I. Rech, "Fully integrated active quenching circuit driving custom-technology spads with 6.2-ns dead time," *IEEE Photonics Technology Letters*, vol. 31, no. 1, pp. 102–105, Jan 2019.

[53] D. Bronzi, S. Tisa, F. Villa, S. Bellisai, A. Tosi, and F. Zappa, "Fast sensing and quenching of cmos spads for minimal afterpulsing effects," *IEEE Photonics Technology Letters*, vol. 25, no. 8, pp. 776–779, April 2013.

[54] A. Katz, T. Blank, A. Fenigstein, T. Leitner, Y. Nemirovsky, and Fellow, "Active-reset for the n+p single-ended spad used in the nir lidar receivers," *IEEE Transactions on Electron Devices*, pp. 1–5, 2019.

[55] F. Zappa, A. Lotito, A. C. Giudice, S. Cova, and M. Ghioni, "Monolithic active-quenching and active-reset circuit for single-photon avalanche detectors," *IEEE Journal of Solid-State Circuits*, vol. 38, no. 7, pp. 1298–1301, July 2003.

[56] A. Rochas, "Single photon avalanche diodes in cmos technology," Ph.D. dissertation, Lausanne, 2003. [Online]. Available: http://infoscience.epfl.ch/record/33289

[57] S. Cova, A. Lacaita, and G. Ripamonti, "Trapping phenomena in avalanche photodiodes on nanosecond scale," *IEEE Electron Device Letters*, vol. 12, no. 12, pp. 685–687, Dec 1991.

[58] M. W. Fishburn, "Fundamentals of cmos single-photon avalanche diodes," Ph.D. dissertation, Delft University of Technology, 2012.

[59] R. D. Yates and D. J. Goodman, *Probability and stochastic processes*. John Wiley & Sons, Inc., 2005.

[60] S. H. Lee, M. Jae, and R. P. Gardner, “Non-poisson counting statistics of a hybrid g–m counter dead time model,” *Nuclear Instruments and Methods in Physics Research Section B: Beam Interactions with Materials and Atoms*, vol. 263, no. 1, pp. 46 – 49, 2007, industrial Radiation and Radioisotope Measurement Applications. [Online]. Available: http://www.sciencedirect.com/science/article/pii/S0168583X07007999

[61] J. van den Broek, “Design and implementation of an analog-to-time-to-digital converter,” *Master’s thesis, Faculty of Electrical Engineering, Mathematics and Computer Science, University of Twente Chair of Integrated Circuit Design*, 2012.

[62] M. Integrated, “MAX35101 Time-to-Digital Converter with Analog Front-End,” https://datasheets.maximintegrated.com/en/ds/MAX35101.pdf, [Online; accessed 20-02-2019].

[63] A. AG, “AS6501 Time-to-Digital Converter,” https://ams.com/as6501#tab/documents, [Online; accessed 20-02-2019].

[64] ——, “TDC-GPX2 Time-to-Digital Converter,” https://ams.com/tdc-gpx2#tab/documents, [Online; accessed 20-02-2019].

[65] T. Instruments, “TDC7201 Time-to-Digital Converter for Time-of-Flight applications,” http://www.ti.com/product/TDC7201/description, [Online; accessed 20-02-2019].

[66] ACAM, “Universal 2-channel Time-to-Digital-Converter,” https://www.pmt-fl.com/uploads/2017/09/precision-measurement-db-gp22-en.pdf, [Online; accessed 20-02-2019].

[67] R. R. Johnson, “Electronic counter,” Patent 3 030 581, April, 1962. [Online]. Available: https://patents.google.com/patent/US3030581A/en

[68] E. Angelopoulou, “The reflectance spectrum of human skin,” 02 2000.

[69] M. J. Mendenhall, A. S. Nunez, and R. K. Martin, “Human skin detection in the visible and near infrared,” *Appl. Opt.*, vol. 54, no. 35, pp. 10 559–10 570, Dec 2015. [Online]. Available: http://ao.osa.org/abstract.cfm?URI=ao-54-35-10559

[70] Pedrotti, Frank L. and Pedrotti, Leno S, *Introduction to Optics, 3d edition*. Englewood Cliffs, N.J. : Prentice Hall, 1932.

[71] R. Otte, L. P. de Jong, and A. H. M. van Roermund, *Low-Power Wireless Infrared Communications*. Springer US, 1999. [Online]. Available: https://doi.org/10.1007/978-1-4757-3015-9

[72] C. Kyba, A. Mohar, and T. Posch, “How bright is moonlight?” *Astronomy & Geophysics*, vol. 58, pp. 1.31–1.32, 02 2017.

[73] N. O. A. Observatory, “Recommended light levels (illuminance) for outdoor and indoor venues,” https://www.noao.edu/education/QLTkit/ACTIVITY_Documents/Safety/LightLevels_outdoor+indoor.pdf, 2015, [Online; accessed 2019-09-13].

[74] Australian Greenhouse Office (May 2005), “Chapter 5: Assessing lighting savings. Working Energy Resource and Training Kit: Lighting,” https://web.archive.org/web/20070415151053/http://www.greenhouse.gov.au/lgmodules/wep/lights/training/training9.html, 2007, [Online; archived from the original on 2007-04-15; Retrieved 2019-09-13].

[75] Paul Darlington, “London Underground: Keeping the lights on,” https://web.archive.org/web/20181116020106/https://www.railengineer.uk/2017/12/05/london-underground-keeping-the-lights-on/, 2017, [Online; archived from original on 2018-11-16; Retrieved 2019-09-13].

[76] ArcGIS Geographical Information System, “Modeling solar radiation,” https://pro.arcgis.com/en/pro-app/tool-reference/spatial-analyst/modeling-solar-radiation.htm, 2019, [Online; accessed 9-October-2019].

[77] C. van den Bos, “Spad signal processing for range finding,” July 2019, private communication.

[78] *Ratio Squarer*, November 1954.

[79] C. van den Bos, “Scope waveforms,” October 2019, private communication.

[80] M. Richards, *Fundamentals of Radar Signal Processing*, 01 2014.

[81] Millind Mittal and Alex Peleg and Uri Weiser, “MMX Technology Architecture Overview,” https://www.intel.com/content/dam/www/public/us/en/documents/research/1997-vol01-iss-3-intel-technology-journal.pdf, 1997, [Online; accessed 05-11-2019].

[82] James Wang, “NVIDIA’s Next Generation CUDA Compute Architecture: Fermi,” https://www.nvidia.com/content/PDF/fermi_white_papers/NVIDIAFermiComputeArchitectureWhitepaper.pdf, 2009, [Online; accessed 14-11-2019].

[83] A.J. Guillon, YetiWare Inc, “An Introduction to OpenCL C++,” https://www.khronos.org/assets/uploads/developers/resources/Intro-to-OpenCL-C++-Whitepaper-May15.pdf, 2015, [Online; accessed 14-11-2019].

[84] C. So-Ling and Ling Li, “A multi-layered reflection model of natural human skin,” in *Proceedings. Computer Graphics International 2001*, July 2001, pp. 249–256.

[85] L. Li and C. S.-L. Ng, “A physically-based human skin reflection model,” in *Proceedings of the 10th WSEAS International Conference on Automation & Information*, ser. ICAI’09. Stevens Point, Wisconsin, USA: World Scientific and Engineering Academy and Society (WSEAS), 2009, pp. 25–30. [Online]. Available: http://dl.acm.org/citation.cfm?id=1562010.1562022

[86] K. J. Dana, S. K. Nayar, B. van Ginneken, and J. J. Koenderink, “Reflectance and texture of real-world surfaces,” in *Proceedings of IEEE Computer Society Conference on Computer Vision and Pattern Recognition*, June 1997, pp. 151–157.

[87] S. K Nayar and M. Oren, “Visual appearance of matte surfaces,” *Science (New York, N.Y.)*, vol. 267, pp. 1153–6, 03 1995.

[88] M. Oren and S. K. Nayar, “Generalization of the lambertian model and implications for machine vision,” *International Journal of Computer Vision*, vol. 14, no. 3, pp. 227–251, Apr 1995. [Online]. Available: https://doi.org/10.1007/BF01679684

[89] University Corporation for Atmospheric Research, “Carbon dioxide 400 ppm atmospheric concentration diagrams,” https://scied.ucar.edu/carbon-dioxide-400-ppm-diagram://scied.ucar.edu/carbon-dioxide-400-ppm-diagrams, 2012, [Online; accessed 12-September-2019].

[90] C. A. Gueymard, “The sun’s total and spectral irradiance for solar energy applications and solar radiation models,” *Solar Energy*, vol. 76, no. 4, pp. 423 – 453, 2004. [Online]. Available: http://www.sciencedirect.com/science/article/pii/S0038092X03003967

[91] E. Shettle and R. Fenn, “Models for the aerosols of the lower atmosphere and the effects of humidity variations on their optical properties,” *Environ. Res.*, p. 94, 09 1979.

[92] E. Tech, “Pololu VL53L0X Time-of-Flight Distance Sensor Carrier with Voltage Regulator, 200cm Max,” https://www.exp-tech.de/en/sensors/distanceapproximation/7557/pololu-vl53l0x-time-of-flight-distance-sensor-carrier-with-voltage-regulator-200cm-max, [Online; accessed 02-12-2019].